

# A novel quantum machine learning classifier to search for new physics

Ji-Chong Yang,<sup>\*</sup> Shuai Zhang, and Chong-Xing Yue<sup>†</sup>

*Department of Physics, Liaoning Normal University, Dalian 116029, China and*

*Center for Theoretical and Experimental High Energy Physics,*

*Liaoning Normal University, Dalian 116029, China*

(Dated: April 18, 2025)

arXiv:2410.18847v3 [hep-ph] 17 Apr 2025

# Abstract

Due to the success of the Standard Model (SM), it is reasonable to anticipate that the signal of new physics (NP) beyond the SM is small. Consequently, future searches for NP and precision tests of the SM will require high luminosity collider experiments. Moreover, as precision tests advance, rare processes with many final-state particles require consideration which demand the analysis of a vast number of observables. The high luminosity produces a large amount of experimental data spanning a large observable space, posing a significant data-processing challenge. In recent years, quantum machine learning has emerged as a promising approach for processing large amounts of complex data on a quantum computer. In this study, we propose quantum searching neighbor (QSN) and variational QSN (VQSN) algorithms to search for NP. The QSN is a classification algorithm. The VQSN introduces variation to the QSN to process classical data. As applications, we apply the (V)QSN in the phenomenological study of the NP at the Large Hadron Collider and muon colliders. The results indicate that the VQSN demonstrates superior efficiency to a classical counterpart k-nearest neighbor algorithm, even when dealing with classical data.

## I. INTRODUCTION

The standard model (SM) is supported by a substantial body of experimental evidence and can be concluded to describe and explain the majority of phenomena in particle physics, with a few rare exceptions. These exceptions include experimental results such as the neutrino mass [1–3], the  $W$  boson mass [4, 5], the muon anomalous magnetic moment ( $g-2$ ) [6–8], and other issues remain unresolved [9]. Furthermore, the SM is unable to account for the existence of dark matter and the force of gravity. Consequently, there is a widely held belief in the existence of new physics (NP) beyond the SM, and the search for NP and precision tests of the SM have become a prominent area of interest within the high-energy physics (HEP) community [10]. Given the success of the SM, it is reasonable to posit that any NP signals that have yet to be discovered will be exceedingly weak. Therefore, the search for NP and the precision tests of the SM motivate higher luminosity collider experiments. The processing of large amounts of data is inherent to such experiments, and thus

---

\* [yangjichong@lnnu.edu.cn](mailto:yangjichong@lnnu.edu.cn)

† [cxyue@lnnu.edu.cn](mailto:cxyue@lnnu.edu.cn); Corresponding author

places demands on our ability to process large amounts of data efficiently.

The application of machine learning (ML) algorithms represents a promising avenue for the efficient processing of data. Its applications have already been demonstrated in HEP [11–23]. Of particular interest in the study of NP phenomenology is the employment of the anomaly detection (AD) algorithms, which have emerged as a prominent area of research in recent years [24–29]. Since ML methods often eliminate the need for detailed kinematic analysis, their benefits become increasingly evident as kinematics grow more complex. Consequently, the advantages will become increasingly apparent as further advances in the precision tests of the SM will inevitably involve the study of rare processes with larger numbers of particles in the final states.

In the meantime, quantum computing represents another effective approach for processing large volumes of data. Despite quantum computing currently being in the noisy intermediate-scale quantum (NISQ) [30–32] era, there has been a notable increase in research activity within the HEP community related to this field [33–52]. Many ML algorithms can be implemented by quantum computing [53–55]. In conjunction with the advancement of quantum ML algorithms, there has been a growing interest in the deployment of quantum ML in the HEP phenomenological studies, encompassing techniques such as variational quantum classifier (VQC) [56–59], quantum support vector machine (QSVM) [56, 60–62], and quantum kernel k-means (QKKM) [63]. In this study, we propose a variational quantum searching neighbor (VQSN) algorithm for identifying NP signals.

To illustrate our algorithm, the SM effective field theory (SMEFT) [64–67] are used as the test cases. The SMEFT has recently been employed extensively in the search for NP. When the collision energy is insufficient to excite NP particles, the NP particles can be integrated out, and the NP effects become new interactions of known particles. These interactions are formally represented as higher-dimensional operators with Wilson coefficients suppressed by powers of a NP scale, denoted as  $\Lambda$ . The signals of the operators that are most likely to be found correspond to those with Wilson coefficients least suppressed by  $\Lambda$ . Instead of dealing with various NP models, the number of operators to be considered at a specific order of  $\Lambda$  is finite. Moreover, if an operator is not found, all NP models contributing to this operator can be constrained. Therefore, the use of the SMEFT is in line with the theme of high efficiency in this work. The present study will investigate the utility of VQSN for the search for high operators at the large hadron collider (LHC) and future muon colliders.

VQSN demonstrates superior performance compared to a classical k-nearest neighbor (KNN) algorithm, even when applied to classical datasets.

## II. SEARCHING FOR NEIGHBORS

In the search for NP, the data to be dealt with are the collision events. The idea of this work is to decide whether some unknown events are neighbors of the SM events, or the NP events. The neighbor events can be defined as soon as the distance between two events is defined. In the case of HEP, there are different methods to define the distance between two events, which can have an impact on the results of event selection strategies [68]. In this work, the observables of final-state particles in one collision event are mapped to a quantum state, and we use a quantum computing friendly way, i.e. the overlap between two states to define distance.

### A. The circuit to search for neighbors

A circuit can be constructed to find the vectors with higher probabilities for closer neighbors. The first step is to construct  $|\psi_n\rangle_a|n\rangle_b$  which can be realized using amplitude encoding, the subscript ‘a’ and ‘b’ denote the corresponding registers for clarity. When the  $|\psi_n\rangle_a|n\rangle_b$  state is created, apply on register  $a$  the inverse of the circuit to amplitude encode  $|\phi\rangle_a$ . And then deduct measurements on the  $a$  register, when the outcome is  $|0\rangle$ , the state obtained is then  $|0\rangle_a \sum_n \langle\phi|\psi_n\rangle|n\rangle$ . The success rate (denoted as  $r$ ) to create the state is  $r = \sum |\langle\phi|\psi_n\rangle|^2 / N$ , where  $N$  is the number of  $\psi_n$  vectors. When  $|0\rangle_a \sum_n \langle\phi|\psi_n\rangle|n\rangle_b$  is obtained, a measurement on  $b$  register will result in  $n$  with the probability proportional to  $|\langle\phi|\psi_n\rangle|^2$ , therefore,  $|n\rangle$  will be obtained with higher probabilities if  $\psi_n$  are closer to  $\phi$ . Denoting the amplitude encoding circuits as  $U_{|\psi_n\rangle|n\rangle}$  and  $U_{|\phi\rangle}$ , i.e.,  $U_{|\psi_n\rangle|n\rangle}|0\rangle = |\psi_n\rangle|n\rangle$  and  $U_{|\phi\rangle}|0\rangle = |\phi\rangle$ , a summary of the circuit to create  $\langle\phi|\psi_n\rangle|n\rangle$  is depicted in Fig. 1. (a). In this work, we use the uniform rotation gates [69] to implement the amplitude encoding.

Without assumptions on the distribution of the vectors, there is no reason to prefer any result of the measurement on  $a$  register. Therefore, if the vectors are  $d$ -dimensional complex vectors,  $r \approx 1/d$ , which is verified by using complex uniform random numbers. The success rate can be improved to  $r \approx 1/\sqrt{d}$  by amplitude amplification, or the ‘QSearch’ algorithm

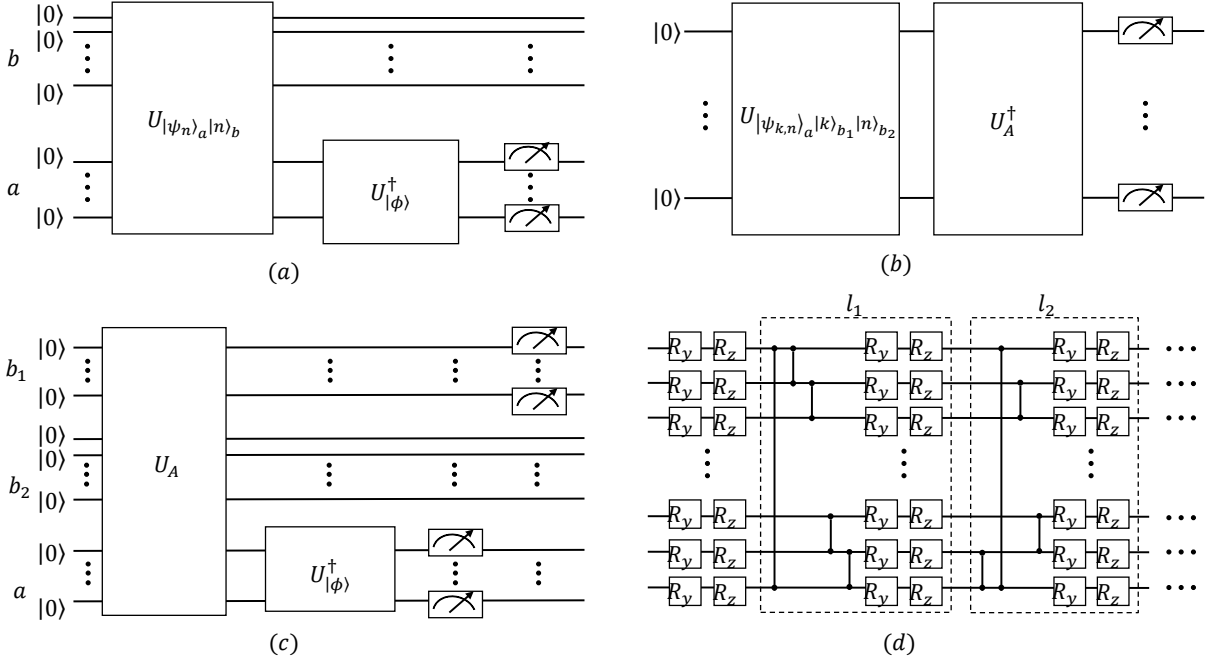


FIG. 1. The circuits used in this paper. The top left panel shows the circuit to construct  $\langle \phi | \psi_n \rangle |n\rangle$ . The top right panel shows the circuit to fit the ansatz. The bottom left panel shows the circuit to find the classification assignment of  $|\phi\rangle$ . The bottom right panel shows an example of ‘hardware efficient’ ansatz used in this paper.

[70].

## B. Fitting the training set

In this work,  $|\psi_n\rangle|n\rangle$  represent events that would be generated by a Monte Carlo (MC) simulation. Since at present, there is no quantum MC algorithm to generate events, one has to deal with a classical dataset. An improvement is to approximate the state  $|\psi_n\rangle|n\rangle$  with a parameterized ansatz circuit.

Since our goal is to classify, in the following, we assume that each  $\psi$  vector carries a classification label and that the states are stored accordingly. Thus, the state to be amplitude encoded is  $|\psi_{k,n}\rangle_a|k\rangle_{b_1}|n\rangle_{b_2}$ , where  $k$  indicates the class. Denoting the circuit of the ansatz as  $U_A(\alpha_i)$  where  $\alpha_i$  are trainable parameters, the circuit of fitting an ansatz is shown in Fig. 1. (b), where the probability of the outcome  $|0\rangle$  in the measurements is

$|\langle \Psi(\alpha_i) | \psi_{k,n} \rangle |k\rangle_{b_1} |n\rangle_{b_2}|^2$  with  $U_A(\alpha_i)|0\rangle = |\Psi(\alpha_i)\rangle$ . The training process adjusts the parameters  $\alpha_i$  to maximize the probability of obtaining  $|0\rangle$  in the measurements.

### C. Variation quantum searching neighbor algorithm

To summarize, the steps of the VQSN are listed as follows,

1. Arrange the training dataset as  $|\psi_{k,n}\rangle_a |k\rangle_{b_1} |n\rangle_{b_2}$ , where  $k$  is the class of  $\psi_{k,n}$ ,  $n$  is the index of  $\psi_{k,n}$  in class  $k$ .
2. Using an ansatz circuit  $|\Psi(\alpha_i)\rangle$  to fit  $|\psi_{k,n}\rangle_a |k\rangle_{b_1} |n\rangle_{b_2}$ .
3. For a test vector  $\phi$ , apply the inverse of amplitude encoding for  $|\phi\rangle_a$  after the ansatz circuit, then measure register  $a$ . If  $|0\rangle_a$  is measured, the state is successfully created. Apply amplitude amplification if necessary.
4. Measure the  $b_1$  register to find out the classification. Similarly to the KNN, we use a majority voting strategy, whereby we repeat  $c$  times and designate the classification of  $\phi$  as the majority result.

In the case of QSN the step-2 is omitted and the exact  $\langle \phi | \psi_{k,n} \rangle |k\rangle_{b_1} |n\rangle_{b_2}$  is created. The circuit of VQSN is shown in Fig. 1. (c).

In essence, the VQSN is a variant of the VQC algorithms. However, it possesses two advantages. Firstly, conventional VQC can be seen as the quantum analogue of an artificial neural network, which is a ‘black box’ difficult to interpret. In contrast, the state to build in QSN has a discernible geometric interpretation, and the target of the training is guaranteed to exist. Secondly, VQSN is accompanied by a classical algorithm, KNN, which allows for a comparison between quantum and classical algorithms. This is clearer for a binary classification problem, in which QSN can be viewed as using  $\sum w_n t_n / N$  to determine the classification of  $\phi$  where  $w_n = |\langle \phi | \psi_n \rangle|^2$ , and  $t_n = 0, 1$  is the class of  $\psi_n$ . Therefore, it uses a weighted average of the entire training dataset. KNN can also be viewed as a weighted average except that  $\{w_n = 1 | \psi_n \in S\}$  and  $\{w_n = 0 | \psi_n \notin S\}$ , where  $S$  is the set contains the  $k$  nearest  $\psi_n$  vectors to  $\phi$ .

### D. A numerical example

Before moving on to the search for NP, a numerical example is implemented to illustrate the algorithm. We use the ‘hardware efficient’ ansatz [71, 72] with the pairwise entanglement layer,

$$U_A(\alpha_i) = \prod_i^l \left( \prod_q e^{i\rho_i^{(q)}\sigma_z^{(q)}} \prod_q e^{i\beta_i^{(q)}\sigma_y^{(q)}} \prod_{\langle q_1, q_2 \rangle} c_z^{q_1, q_2} \right) \times \prod_q e^{i\rho_0^{(q)}\sigma_z^{(q)}} \prod_q e^{i\beta_0^{(q)}\sigma_y^{(q)}}, \quad (1)$$

where  $\sigma_{y,z}^q$  are Pauli matrices acting on  $q$  qubit, the product over  $q$  is the product over all qubits,  $c_z^{q_1, q_2}$  is the controlled-Z gate acting on  $q_{1,2}$  qubits with  $c_z = \text{diag}(1, 1, 1, -1)$ , and  $\langle q_1, q_2 \rangle$  is the set of pairs of qubits depending on the type of entanglement layer,  $l$  is the number of layers of the ansatz,  $\{\alpha_i\} = \{\beta_0^{(q)}, \rho_0^{(q)}, \beta_1^{(q)}, \rho_1^{(q)}, \dots, \beta_l^{(q)}, \rho_l^{(q)}\}$  is a set of trainable parameters. The number of parameters is  $2(l+1)n_q$  where  $n_q$  is the number of qubits.  $U_A$  is shown in Fig. 1. (d).

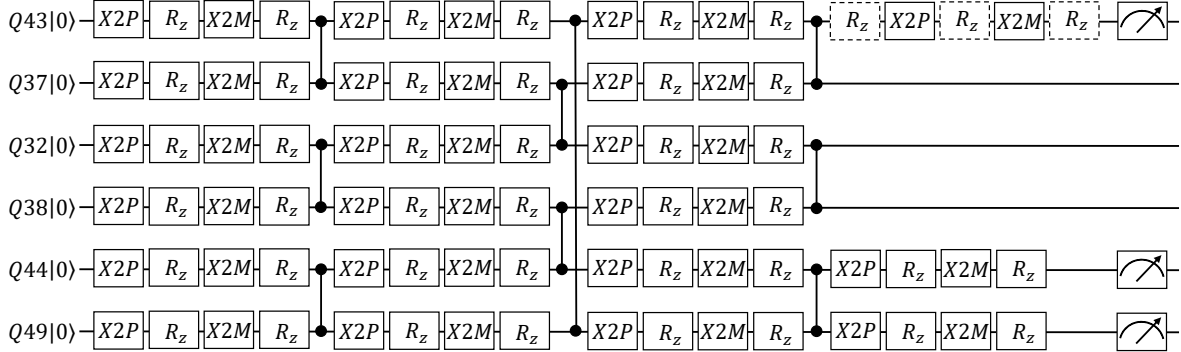


FIG. 2. The circuit running on *tiyanan176-2* to classify a test point. The  $X2M$  is  $R_x(-\pi/2)$  gate,  $X2P$  is  $R_x(\pi/2)$  gate. The parameters of the gates depicted using dashed edged boxes are different for different test points. The parameters of the gates depicted using solid edged boxes are the same because they are used to build the ansatz. The  $Q43$  is  $a$  register,  $Q44$  and  $Q49$  make up the  $b_1$  register, and the others make up the  $b_2$  register.

In the numerical example, we use  $N = 32$  two dimensional points which are divided into four classes equally. The training set is generated using `scikit-learn` [73], and  $x, y$

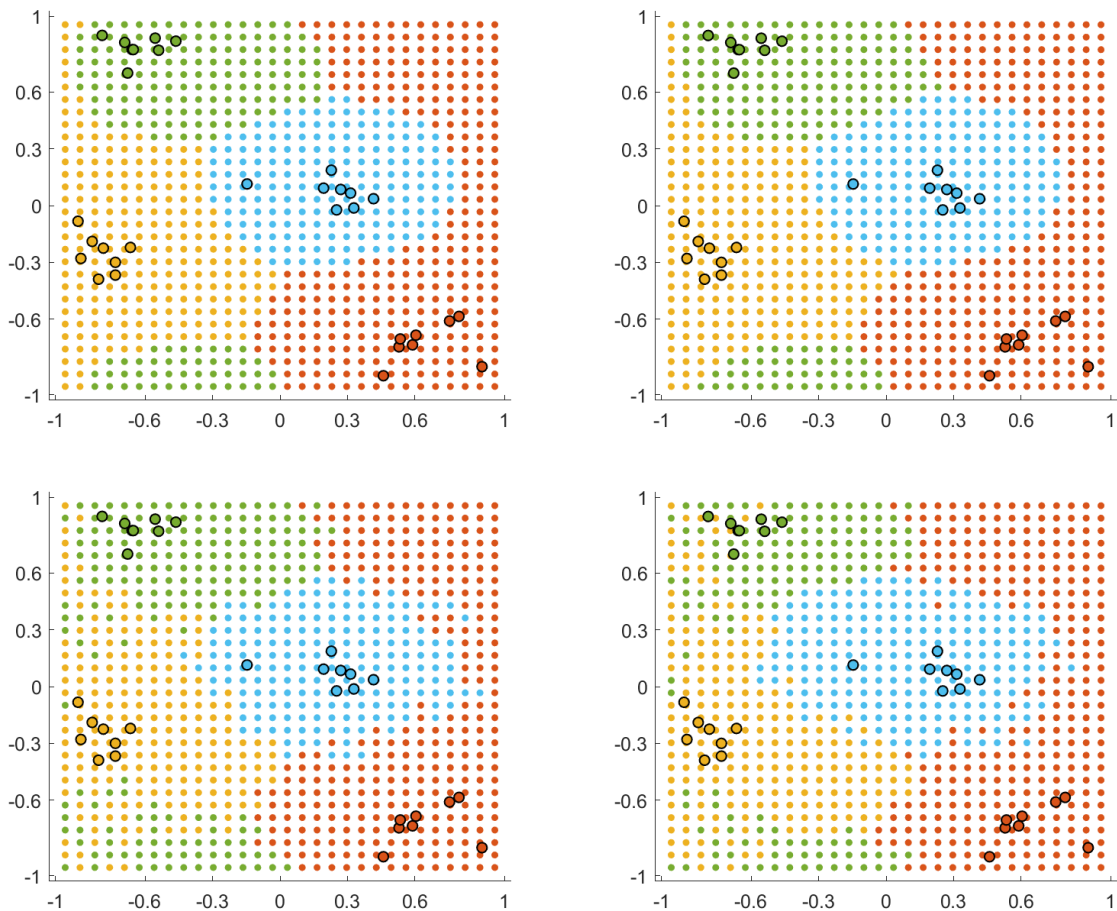


FIG. 3. The example of classifier with two dimensional vectors. The top left panel is the result of QSN with  $c \rightarrow \infty$  (with direct comparison of probabilities of each amplitudes). The top-right panel is the result of VQSN with  $l = 3$  and  $c \rightarrow \infty$ . The bottom-left panel is the result of VQSN with  $l = 3$  and  $c = 1000$ . The bottom-right is the result of VQSN on *tianyanyan176-2* with  $l = 3$  and  $c = 1000$ .

coordinates are translated as zenith and azimuth angles of the Bloch sphere,  $\theta = (x + 1)\pi/2$ ,  $\varphi = (y + 1)\pi$ . When training, we use ‘Adam’ optimizer [74], and the initialization of the ansatz parameters is randomly sampled from the many-body localized distribution [75], the training is done by using the QuEST toolkit [76]. When  $l = 3$ , the ansatz is trained to a fidelity of 99.4%. In terms of quantum control instruction set (QCIS), the circuit for classification is depicted in Fig. 2. Then we scan the Bloch sphere and use QSN and VQSN to determine the classification assignment of each point on the Bloch sphere. The discrimination circuit

is also run on *tianyan176-2* of *Tianyan quantum computing cloud platform*, with *Zuchongzhi* superconducting quantum computing system [77].

The training set and the results with different methods are shown in Fig. 3. The difference between the QSN and VQSN with  $c \rightarrow \infty$  indicates the effect of approximation of  $|\Phi\rangle$  with an ansatz. The difference between the VQSN with  $c \rightarrow \infty$  and  $c = 1000$  indicates the effect of randomness in measurements. The difference between the results obtained by QuEST and *tianyan176-2* indicates the effect of noise on a quantum computer. It can be shown that (V)QSN works as expected, the VQSN demonstrates resilience to noise, and the primary error originates from the randomness in measurements.

### III. APPLICATIONS IN THE SEARCH FOR NEW PHYSICS

The searching for NP signals can be considered as a binary classification, therefore the (V)QSN is expected to be feasible in the phenomenological study of NP. In this section, three applications to use (V)QSN to search for NP and set expected constraints on the NP parameters are present.

#### A. Preparation of the datasets

The datasets are generated using MadGraph5 toolkit[78–80]. A parton shower is applied using Pythia8 with NNPDF [81, 82], the fast detector simulation is applied using Delphes [83] with either the CMS or muon collider card, depending on the processes under study. The preparation of the datasets are applied using MAnalysis [84].

After the collision events are generated, a set of observables are picked to form the feature space, an event can be mapped into this feature space as a vector  $\vec{v}$ . Assuming  $D$  observables are picked, then  $\vec{v}$  is a  $D$ -dimensional vector. The z-score standardization [85] is applied,  $x_m^j = (v_m^j - \bar{v}^j) / \epsilon^j$ , where  $v_m^j$  is the  $j$ -th component ( $0 \leq j \leq D - 1$ ) of  $\vec{v}_m$  for the  $m$ -th collision event,  $\bar{v}^j$  and  $\epsilon^j$  are mean values and standard deviations of the  $j$ -th component of  $\vec{v}$  over the training dataset.

To map the above vector to a quantum state, we use amplitude encoding,

$$|\psi_m\rangle = \frac{1}{\sqrt{1 + \sum_{j=0}^{d-1} (x_m^j)^2}} \left( \sum_{j=0}^{d-1} (x_m^{2j} + x_m^{2j+1}i) |j\rangle \right), \quad (2)$$

where  $d$  is the least power of 2 larger than  $d'/2$ , for  $x_m^j$  with  $j > D-1$ ,  $x_m^{j=d'} = 1$  and  $x_m^{j>d'} = 0$  are used. The encoding in Eq. (2) is for convenience. This study has not addressed further improvements such as encoding the vectors in the dataset into a quantum state using a nonlinear approach [86]. It is also possible to utilize the vast Hilbert space of quantum computers to separate the signal from the background more when mapping to the quantum feature space [87].

## B. Event selection strategy

The search for NP is binary classification, therefore we change the last step of (V)QSN in Sec. II C. Denoting  $|\psi_{n,\text{SM}}\rangle$  and  $|\psi_{n,\text{NP}}\rangle$  as states for the SM and NP events, respectively, the state to be trained is arranged as,

$$\Psi_{\text{train}} = \sum_n^{\frac{N}{2}} (|\psi_{n,\text{NP}}\rangle_a |0\rangle_{b_1} |n\rangle_{b_2} + |\psi_{n,\text{SM}}\rangle_a |1\rangle_{b_1} |n\rangle_{b_2}). \quad (3)$$

The number of  $|0\rangle_{b_1}$  outcome is denoted as  $a$  and  $\hat{a} = a/(rc)$  is used as a score to indicate the probability such how likely  $\phi$  is from the NP, where  $r \times c$  is the number of times  $\langle\phi|\Psi\rangle$  is successfully built. And after  $\hat{a}$  is obtained, we select events with  $\hat{a} > \hat{a}_{th}$  where  $\hat{a}_{th}$  is a tunable threshold that maximizes the signal significance which is defined as [88, 89],

$$\mathcal{S}_{stat} = \sqrt{2[(N_{bg} + N_s) \ln(1 + N_s/N_{bg}) - N_s]}, \quad (4)$$

where  $N_{bg}$  and  $N_s$  are number of background and signal events, respectively, and  $N_{s,bg} = L\sigma_{s,bg}$ , where  $L$  is the luminosity,  $\sigma_{s,bg}$  are the cross-sections of signal and background contributions. The accuracy of  $\hat{a}$  can be estimated as  $\mathcal{O}(1/\sqrt{rc})$ .

For comparison with a classical algorithm, we also introduce the classical KNN algorithm which is already used in the search for NP [22]. We use a modified KNN (denoted as ‘t-KNN’ where ‘t’ stands for tunable) with the following strategy for event selection.

1. For a data point in the test dataset, find the  $k$  closest data points to this point in the training set.
2. Among these  $k$  points, find out how many of them are from the NP, assuming the number of those points is  $b$ , use  $\hat{b} = b/k$  as the anomaly score for the point being tested.

3. Determine a tunable threshold  $\hat{b}_{th}$  according to signal significance, and select the events with  $\hat{b} > \hat{b}_{th}$ .

When  $\hat{b}_{th} = 0.5$ , this is the conventional KNN algorithm. When using the (t-)KNN, the training dataset is the same one as the (V)QSN but consists of  $D$ -dimensional real vectors  $\vec{x}$ . However, when finding the  $k$  closest data points, we use the Euclidean distance.

For the (t-)KNN algorithm, we only incorporate the cost needed to compute the distances, so the computational complexity (cc) can be estimated as  $\mathcal{O}(d'NM)$  for  $M$  test events. In the context of quantum computers, the number of quantum gates is typically employed as a means of assessing the cc. Even if the dataset is classical, the cc for VQSN is  $n_t + \mathcal{O}(c'M(n_{ans} + d)\sqrt{d})$ , where  $n_t$  is the cost to train the ansatz which is a constant in the view of test dataset,  $n_{ans}$  is the cc of the ansatz, the cc of  $U_{|\phi}^\dagger$  is  $\mathcal{O}(d)$ , and  $c = c'/\sqrt{d}$  where  $1/\sqrt{d}$  comes from the success rate to create the state  $\langle \phi | \Psi(\alpha_i) \rangle$  when amplitude amplification is used and the number of times of measurement on  $a$  is required to be a fixed number  $c'$ . Note that,  $n_t$  depends on  $N$  and  $d$ , but not on  $M$ . Unlike  $M$  which grows with the luminosity,  $N$  and  $d$  remain effectively constant in practical applications, as a result, for practical applications it can be expected that  $M \gg N$ . By omitting  $n_t$  because  $M \gg N$ , and by the fact that  $d$  is at the same order of  $D$ , it can be estimated that the VQSN outperforms (t-)KNN even with a classical dataset when  $c(n_{ans} + d) < N\sqrt{d}$ . From the principle of the algorithm, the larger  $N$  and  $d$ , the better the classification, as long as  $M \gg N$  is kept, this means that ideally VQSN can outperform (t-)KNN even dealing with a classical dataset.

### C. Search for the gluon quartic gauge couplings at a muon collider

#### 1. The contribution of the gluon quartic gauge coupling at a muon collider

The gluon quartic gauge couplings (gQGCs) emerge from the Born-Infeld (BI) extension of the SM, which was originally driven by the idea that there should be an upper limit on the strength of the electromagnetic field [90]. It has been demonstrated that the BI model is also associated with M-theory-inspired models [91–95]. In the SMEFT, the operators contributing to gQGCs appear at dimension-8. As the importance of the dimension-8 operators in the SMEFT has been realized [96–101], more and more phenomenological studies have been devoted to the dimension-8 operators in recent years [102–123]. The case of gQGC is

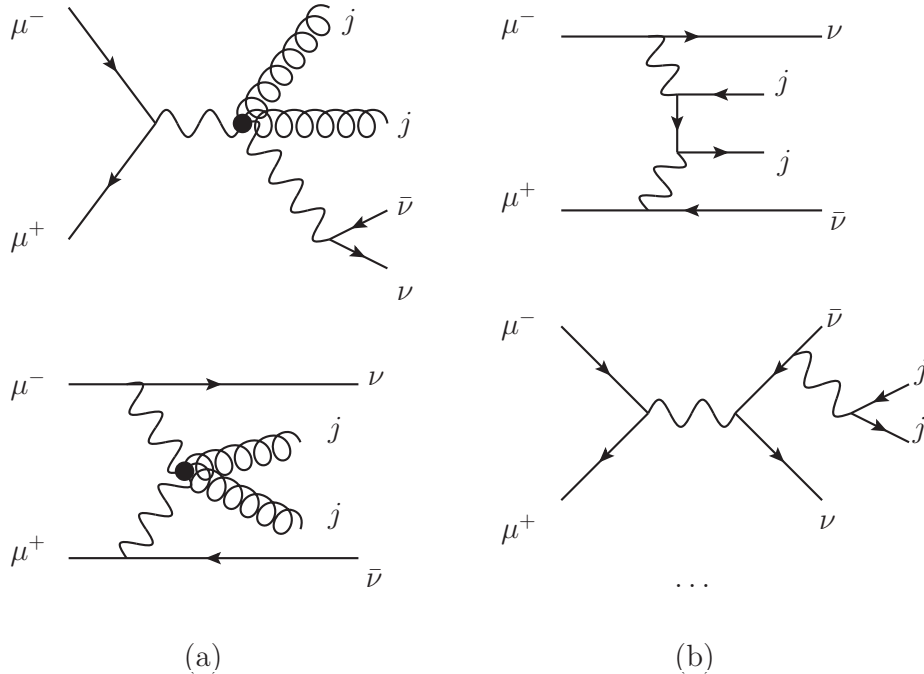


FIG. 4. Feynman diagrams of the process  $\mu^+\mu^- \rightarrow jj\nu\bar{\nu}$  (diagrams in (a) represent the contribution of  $O_{gT,0}$ , while diagrams in (b) represent the SM contribution).

among the operators of dimension-8 in the SMEFT that have received attention. We focus on the  $O_{gT,0}$  operator,

$$O_{gT,0} = \frac{1}{16M_0^4} \sum_a G_{\mu\nu}^a G^{a,\mu\nu} \times \sum_i W_{\alpha\beta}^i W^{i,\alpha\beta}, \quad (5)$$

where  $G_{\mu\nu}^a$  is gluon field strengths,  $W_{\mu\nu}^i$  denote electroweak field strengths, and  $M_0$  is the NP scale. The expected constraints is  $M_0 \geq 1040$  MeV at the LHC with the center of mass (c.m.) energy  $\sqrt{s} = 13$  TeV, and luminosity  $L = 36.7$  fb $^{-1}$  obtained by using the process  $gg \rightarrow \gamma\gamma$  [91]. The combined sensitivities of the  $Z\gamma$  and  $\gamma\gamma$  channels at the LHC with  $\sqrt{s} = 13$  TeV and  $L = 137$  fb $^{-1}$  are about three times of the above [92]. For convenience, we define  $f_0 \equiv 1/(16M_0^4)$ .

At muon colliders, the gQGCs contributes to the process  $\mu^+\mu^- \rightarrow \nu\bar{\nu}jj$  [124]. The Feynman diagrams are shown in Fig. 4. This process is chosen as one of the processes to validate the VQSN since it is convenient to handle due to the absence of interference between the SM and NP.

## 2. Training of the ansatz

	$v^0$	$v^1$	$v^2$	$v^3$	$v^4$	$v^5$
observables	$E_{j_1}$	$p_{j_1}^T$	$E_{j_2}$	$p_{j_2}^T$	$\cancel{E}$	$\cancel{p}^T$

TABLE I. The components of the feature space and the corresponding observables.

The events are generated for a 3 TeV muon collider. The final states are required to contain at least two jets. At lepton colliders, the missing energy is also accessible, the chosen observables are listed in Table I, where  $E_{j_{1,2}}$  and  $p_{j_{1,2}}^T$  are the energies and transverse momenta of the hardest and second hardest jets,  $\cancel{E}$  is the missing energy, and  $\cancel{p}^T$  is the transverse missing momentum, respectively. Therefore, in this case,  $d' = 6$  and  $d = 4$ .

$2^{17} + 2^{17}$  events are selected from the SM and NP events to form the training set. Since the  $XY2M(\theta) = R_z(\theta)R_x(-\pi/2)R_z(-\theta)$  and  $XY2P(\theta) = R_z(\theta)R_x(\pi/2)R_z(-\theta)$  are supported gates on *tianyan176-2*, the single qubit layer of the ansatz are chosen to be  $XY2M(\theta_1)XY2P(\theta_2)$  on each qubit. The entanglement layer is chosen to be pairwise. The ansatz is chosen to have  $l = 3$  entanglement layers, with  $N = 2^{18}$  and  $d = 4$ ,  $n_q = 20$  qubits are used. The ansatz is trained using QuEST, the fidelity reaches 78.5%.

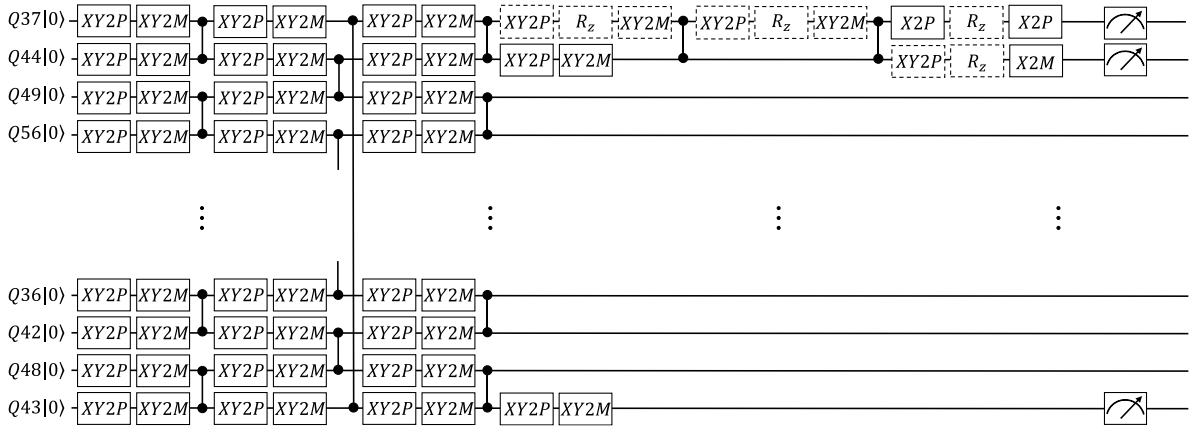


FIG. 5. Same as Fig. 2 but for the study of gQGCs in the process  $\mu^+\mu^- \rightarrow \nu\bar{\nu}jj$ . The Q37 and Q44 make up the  $a$  register, Q43 is the  $b_1$  register, and the others make up the  $b_2$  register.

The test dataset are 50000 + 50000 events selected from the SM and NP contributions, which are all different from the training events. In the case of running on the *tianyan176-2*,

a sub set consist of 500 + 500 events are selected. The circuit for discrimination in terms of QCIS on *tianyan176-2* are shown in Fig. 5.

### 3. Numerical results

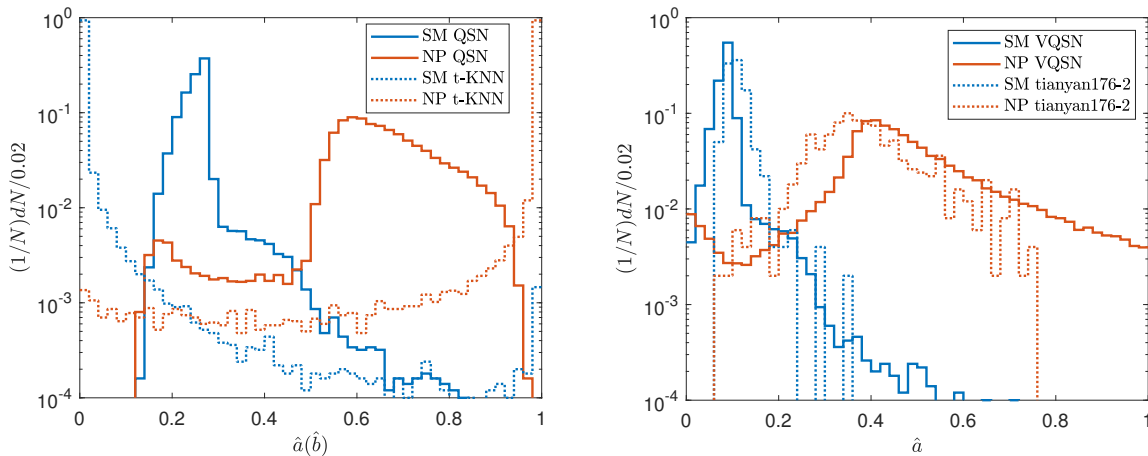


FIG. 6. The normalized distributions of  $\hat{a}$  and  $\hat{b}$  for different methods.

To compare the results, we also use QSN and VQSN with  $c \rightarrow \infty$ , and with (t-)KNN with  $k = 1000$  (the results of  $k = 10, 100$  are similar with the case of  $k = 1000$ ). On *tianyan176-2*, we use  $c = 1000$ . For the test set, the normalized distributions of  $\hat{a}$  and  $\hat{b}$  are shown in Fig. 6. It can be seen that, both  $\hat{a}$  and  $\hat{b}$  can be used for discriminating the NP signals from the SM background. The difference between the QSN and t-KNN comes from the fact that the QSN algorithm weights all points into account, which may bring the two peaks closer. However, QSN also has an advantage that the tail of the SM background at the large  $\hat{a}$  region is suppressed. The difference between QSN and VQSN indicates that both peaks are shifted to a lower  $\hat{a}$  region by VQSN, but the discriminative power is not significantly affected.

The receiver operating characteristic curve (ROC) represents a crucial metric for evaluating the efficacy of a classification algorithm. ROC is obtained by mapping the  $\hat{a}_{th}$  ( $\hat{b}_{th}$ ) into a two-dimensional plane with false positive rate (FPR) and true positive rate (TPR) as axes. The area under the ROC (AUC) can be utilized as a quantitative metric to assess the efficacy of a classification algorithm. The ROCs for (V)QSN and t-KNN are shown in

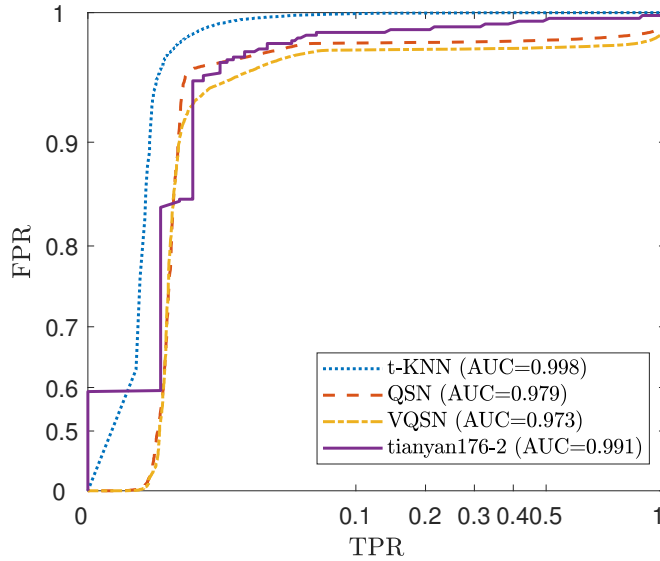


FIG. 7. The ROCs for different event selection strategies and the corresponding AUCs, the  $x$ -axis (TPR) is scaled as  $x^{1/3}$  and the  $y$ -axis (FPR) is scaled as  $y^3$  for clarity.

Fig. 7. The large AUC in the case of *tianyan176-2* can be attributed to the fact that the difference between all cases is small, therefore the results are affected by a limited number of events, and the test set running on *tianyan176-2* consists of only 1% events.

	$\hat{a}_{th}(\hat{b}_{th})$	$\varepsilon_{\text{SM}}$	$\varepsilon_{\text{NP}}$	$\mathcal{S}_{stat} = 2$ ( $\text{TeV}^{-4}$ )	$\mathcal{S}_{stat} = 3$ ( $\text{TeV}^{-4}$ )	$\mathcal{S}_{stat} = 5$ ( $\text{TeV}^{-4}$ )
KNN		0.484%	98.2%	0.194	0.238	0.308
t-KNN	0.003	0.074%	76.43%	0.138	0.170	0.221
QSN	0.44	0.33%	85.29%	0.190	0.233	0.301
VQSN	0.64	0.322%	85.67%	0.189	0.232	0.301
tianyan176-2	0.71	0.2%	82.2%	0.171	0.209	0.271

TABLE II. The  $\hat{a}_{th}$ ,  $\hat{b}_{th}$ , cut efficiencies and the expected coefficient constraints.

The expected constraints on  $|f_0|$  can be obtained by Eq. (4) and,

$$\sigma^{\mu^+\mu^-\rightarrow jj\nu\bar{\nu}}(f_0) = \varepsilon_{\text{SM}}\sigma_{\text{SM}}^{\mu^+\mu^-\rightarrow jj\nu\bar{\nu}} + \frac{f_0^2}{\tilde{f}_0^2}\varepsilon_{\text{NP}}\sigma_{\text{NP}}^{\mu^+\mu^-\rightarrow jj\nu\bar{\nu}}, \quad (6)$$

where  $\sigma_{\text{SM}}^{\mu^+\mu^-\rightarrow jj\nu\bar{\nu}}$  and  $\sigma_{\text{NP}}^{\mu^+\mu^-\rightarrow jj\nu\bar{\nu}}$  are the cross-section of the SM and NP after requiring at least two jets,  $\sigma_{\text{NP}}^{\mu^+\mu^-\rightarrow jj\nu\bar{\nu}}$  is obtained when  $f_0 = \tilde{f}_0$ . At  $\sqrt{s} = 3$  TeV and  $\tilde{f}_0 = 1$   $\text{TeV}^{-4}$ ,

$\sigma_{\text{SM}}^{\mu^+\mu^-\rightarrow jj\nu\bar{\nu}} = 722.9$  fb and  $\sigma_{\text{NP}}^{\mu^+\mu^-\rightarrow jj\nu\bar{\nu}} = 3.21$  fb [124]. By choosing proper  $\hat{a}_{th}$  and  $\hat{b}_{th}$ , the expected constraints on  $|f_0|$  at  $\sqrt{s} = 3$  TeV and  $L = 1$  ab $^{-1}$  (where  $L$  is the luminosity chosen according to the design of the muon colliders [125, 126]) are listed in Table II. The expected constraints on  $|f_0|$  by using a traditional event selection strategy at  $\mathcal{S}_{start} = 2, 3$  and 5 are  $< 0.155, < 0.191$  and  $0.248$  TeV $^{-4}$ , respectively. The dataset in this paper is in fact a subset (about 28%) of the one used in Ref. [124], it can be seen that the VQSN can reach a same order of magnitude, while t-KNN outperforms the traditional method.

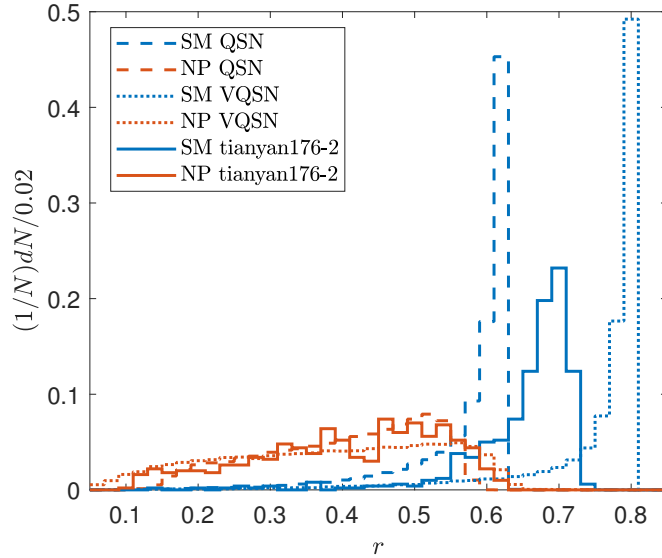


FIG. 8. The normalized distributions of  $r$  for different methods.

It has been shown that, the randomness in measurement contributes to the primary of the errors. In this subsection,  $c = 1000$  is used. When  $c$  is a constant, the accuracy of  $\hat{a}$  is affected by  $r$ , the success rates of building the states  $\langle \phi | \Psi_{\text{train}} \rangle$  and  $\langle \phi | \Psi(\alpha_i) \rangle$  (where  $\phi$  is the state for a test vector). Fig. 8 illustrates the normalized distributions of success rates where  $\phi$  are the signal and background events in the validation dataset. The background and signal events are considered separately because the majority of the dataset from experiments will be the latter. It can be observed that the success rate is typically higher for background events than for signal events. This is due to the more centralized distribution of background events since the success rate is  $\sum_n^N |\langle \phi | \psi_n \rangle|^2 / N$  for QSN. Furthermore, it was found that the ansatz not only did not reduce but rather enhanced the success rates for the background events. This further reduces the cc of VQSN because for a fixed  $c'$ , a smaller  $c$  is needed.

The cc of VQSN and its classical counterpart, i.e. (t-)KNN is compared. For one test event, 168 gates need to be applied in terms of QCIS, therefore, when  $c = 1000$ , the cc is estimated as 168000. For (t-)KNN, the cc is for one test event is  $1.57 \times 10^6$  because the training set contains  $2^{18}$  6-dimensional vectors. It can be seen that, even with a classical dataset, the cc of VQSN can be one order of magnitude smaller.

#### D. Search for the gluon quartic gauge couplings at the LHC

##### 1. The gluon quartic gauge couplings and the process to be considered

One of the reasons muon collider is better suited to the search for NP is that the QCD background is suppressed. ML algorithms are more suitable for processes with more intricate final states, which necessitates greater investment in kinematic analysis when traditional methods are employed. There are certain complexities involved in discussing QCD background at the LHC, which offer an opportunity for utilizing ML algorithms in this regard. Therefore, we also investigate an example of the search for gQGCs at the LHC.

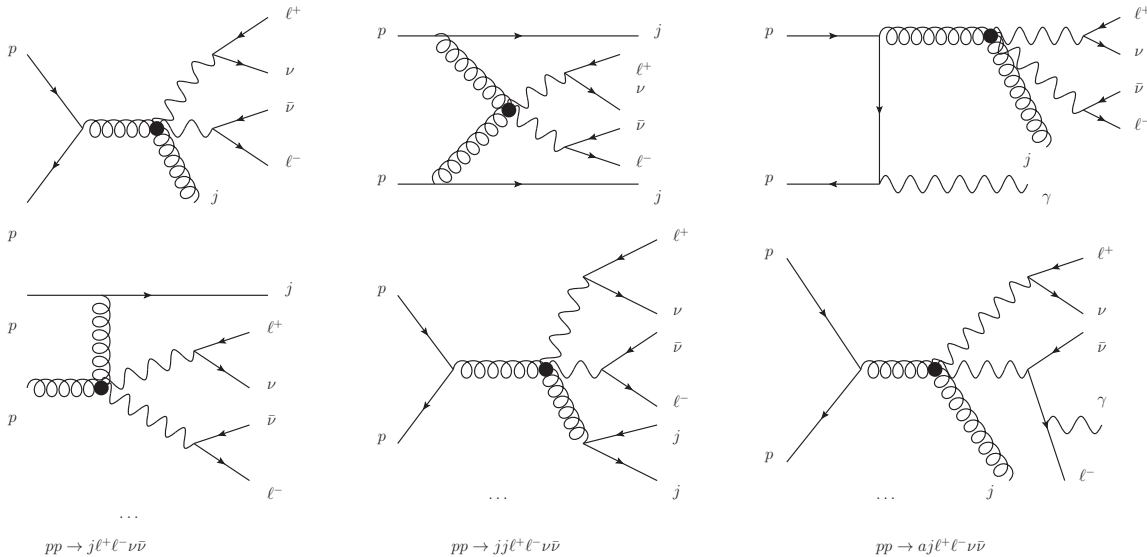


FIG. 9. Feynman diagrams the processes  $pp \rightarrow jl^+\ell^-\bar{\nu}\nu$  (left panels),  $pp \rightarrow jjl^+\ell^-\bar{\nu}\nu$  (middle panels) and  $pp \rightarrow \gamma jl^+\ell^-\bar{\nu}\nu$  (right panels), respectively, induced by the gQGCs.

In this paper, three processes  $pp \rightarrow jl^+\ell^-\bar{\nu}\nu$ ,  $pp \rightarrow jjl^+\ell^-\bar{\nu}\nu$  and  $pp \rightarrow \gamma jl^+\ell^-\bar{\nu}\nu$  are considered together. The Feynman diagrams are shown in Fig. 9. The three processes

	processes	$\sigma$ (pb)
$t\bar{t}$	$pp \rightarrow t\bar{t} + jets$	832
$ll + jets$	$pp \rightarrow jj\ell^+\ell^-$	208
	$pp \rightarrow jjj\ell^+\ell^-$	84.3
	$pp \rightarrow jjj\ell^+\ell^-$	32.9
$jlll\nu$	$pp \rightarrow j\ell^+\ell^-\ell^+\nu$	0.106
	$pp \rightarrow j\ell^+\ell^-\ell^-\bar{\nu}$	0.0703
$\gamma ll + jets$	$pp \rightarrow \gamma j\ell^+\ell^-$	6.51
	$pp \rightarrow \gamma jj\ell^+\ell^-$	2.85

TABLE III. The backgrounds due to mis-tagging, or due to particles missed by the detectors, and their cross-sections.

are combined together because they have similar backgrounds. The presence of two (anti-)neutrinos in the final state inevitably entails a certain degree of information loss, which offers an opportunity to assess the efficacy of our algorithm.

Except for the SM contribution, other processes contributing to background due to detector effects are considered, including  $pp \rightarrow (\gamma)ll + jets$  with missing jets,  $pp \rightarrow t\bar{t} \rightarrow jjW^+W^- \rightarrow jj\ell^+\ell^-\nu\bar{\nu}$  with b-jets mis-tagged, and  $pp \rightarrow jlll\nu$  with a missing charged lepton. They are listed in Table III, with the cross-sections obtained by using MadGraph5 toolkit [78], except for the case of  $t\bar{t} + jets$ , in which we use inclusive cross-section of  $t\bar{t} + jets$  production [127–129].

## 2. Training of the ansatz

To suppress the background with many jets, it is required that the number of jets (denoted as  $N_j$ ) in the final state satisfying  $1 \leq N_j \leq 6$ , and it is required that there is no  $b$ -jet. Furthermore, to suppress the  $pp \rightarrow \ell^+\ell^- + jets$  background, it is required that the transverse missing energy (denoted as  $\cancel{E}_T$ ) satisfying  $\cancel{E}_T > 200$  GeV. Except for that, the final state is required to have exactly two opposite charged leptons. The above requirement is called particle number cut, and is denoted as  $N_{part}$  cut.

A natural way is to use a feature space whose axes are observables in a collision event. As a ML algorithm, instead of analyzing the kinematics, we simply chose some typical

	$v^0$	$v^1$	$v^2$	$v^3$	$v^4$	$v^5$	
observables	$E_{j_1}$	$p_{j_1}^T$	$E_{j_2}$	$p_{j_2}^T$	$E_{\ell^+}$	$p_{\ell^+}^T$	
	$v^6$	$v^7$	$v^8$	$v^9$	$v^{10}$	$v^{11}$	$v^{12}$
observables	$E_{\ell^-}$	$p_{\ell^-}^T$	$E_\gamma$	$p_\gamma^T$	$\cancel{E}_T$	$f_{\ell^+}$	$f_{\ell^-}$

TABLE IV. Same as Table I but for the processes at the LHC.

observables arbitrarily, and the more observables are expected to be better. In this work we mainly use the momentum space of the final particles, i.e., the energies ( $E$ ) and transverse momenta ( $p^T$ ) of the hardest three jets, the hardest photon, and the charged leptons are picked as the features, as well as the missing momentum ( $\cancel{E}_T$ ). Since degrees of freedom of a  $n$ -qubit state is  $2^n - 2$ , to better utilize the Hilbert space, the  $f_{\ell^\pm}$  are added which are the flavors of charged leptons, and  $f_{\ell^\pm} = 0, 1$  when the charged leptons are electron or muon. In summary, an event is mapped into a 13-dimensional vector  $\vec{v}$  whose components are listed in Table IV. If there are no photons or less than three jets, the corresponding  $E_{\gamma, j_i}$  and  $p_{\gamma, j_i}^T$  are set to be zero. Using this feature space,  $d = 8$  and  $d' = 13$ , respectively.

processes	number of events
$pp \rightarrow jj\ell^+\ell^-\nu\bar{\nu}$ for $O_{gT,0}$	16384
$pp \rightarrow j\ell^+\ell^-\nu\bar{\nu}$ for $O_{gT,0}$	12288
$pp \rightarrow \gamma j\ell^+\ell^-\nu\bar{\nu}$ for $O_{gT,0}$	4096
$pp \rightarrow jj\ell^+\ell^-\nu\bar{\nu}$ in the SM	16384
$pp \rightarrow j\ell^+\ell^-\nu\bar{\nu}$ in the SM	8192
$pp \rightarrow t\bar{t} \rightarrow jjW^+W^- \rightarrow jj\ell^+\ell^-\nu\bar{\nu}$	8192

TABLE V. The processes and the number of events included in the training dataset.

The training dataset is consist of events after  $N_{part}$  cut. The number of events picked to form the training dataset is listed in Table V. Training dataset has  $N = 65536$  vectors, with three qubits to encode one vector, with  $d = 8$ , the number of qubits to store  $\Psi_{\text{train}}$  (or the ansatz  $\Psi(\alpha_i)$ ) is  $n_q = 19$ . In this subsection, the ‘shifted-circular-alternating’ (SCA) entanglement layer [130] is used. The circuit of the ansatz is the one shown in Fig. 1. (d).

Without the amplitude amplification, the cc for an ansatz with SCA entanglement layers is about  $((2 + 3l)n_q + 2(2d - \log_2(d) - 2))c'd$  for a test event. In this subsection, the calcu-

lation is performed by using QuEST, taking advantages of the controlled collapse operation of a simulator, we use a fixed  $c' = 100$  for simplicity. If the cc of VQSN is to be less than that of its KNN counterpart (which is  $d'N = 8.5 \times 10^5$  with  $d' = 13$  and  $N = 65536$ ), the ansatz should satisfy  $l < 17.6$ . In this work, we consider three cases,  $l = 5, 10$ , and  $15$ . As a comparison, we consider (t-)KNN with  $k = 1, 10, 100$ , and  $1000$ .

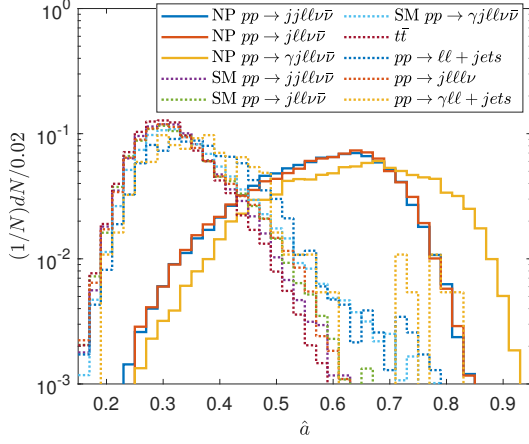
### 3. Numerical results

	processes	$\sigma$ (fb)	$\sigma_{N_{part}}$ (fb)		$\varepsilon_{N_{part}}$
NP	$jj\ell^+\ell^-\nu\bar{\nu}$	1.485	0.7034		47.5%
	$j\ell^+\ell^-\nu\bar{\nu}$	1.549	0.6923		44.6%
	$\gamma j\ell^+\ell^-\nu\bar{\nu}$	0.1738	0.06879		39.5%
SM	$jj\ell^+\ell^-\nu\bar{\nu}$	679.3	16.76		2.47%
	$j\ell^+\ell^-\nu\bar{\nu}$	$1.147 \times 10^3$	14.01		1.22%
	$\gamma j\ell^+\ell^-\nu\bar{\nu}$	18.90	0.3530		1.87%
	$t\bar{t}$	$2.519 \times 10^4$	101.1		0.401%
	$ll + jets$	$3.251 \times 10^5$	44.10		0.0136%
	$jlll\nu$	$1.826 \times 10^3$	0.7914	45.18	0.0433%
	$\gamma ll + jets$	$9.367 \times 10^3$	0.2954		0.00315%

TABLE VI. The cross-sections before cuts ( $\sigma$ ), and the  $N_{part}$  cut ( $\sigma_{N_{part}}$ ), and the cut efficiency of the  $N_{part}$  cut ( $\varepsilon_{N_{part}}$ ) for different processes.

For simplicity, we consider only the cut efficiency of  $pp \rightarrow t\bar{t}$  and evaluate the  $t\bar{t} + jets$  using the inclusive cross-section of the process  $t\bar{t} + jets$  with the cut efficiency of  $pp \rightarrow t\bar{t}$ . The considered signal and background processes and the cross-section after  $N_{part}$  cut are listed in Table VI. The requirement for a minimal  $\cancel{E}_T$  significantly suppresses the background events without neutrinos. In Table VI, the  $b$ -tagging efficiency is assumed to be 77% [131, 132].

After the  $N_{part}$  cut, the ansatz is trained. The fidelities for  $l = 5, 10$  and  $15$  ansatz are 47.12%, 47.47% and 47.53%, respectively. A validation set is made which is consist of events after  $N_{part}$  cut with 73400 and 108000 NP and SM events (all different from the training



(a) QSN

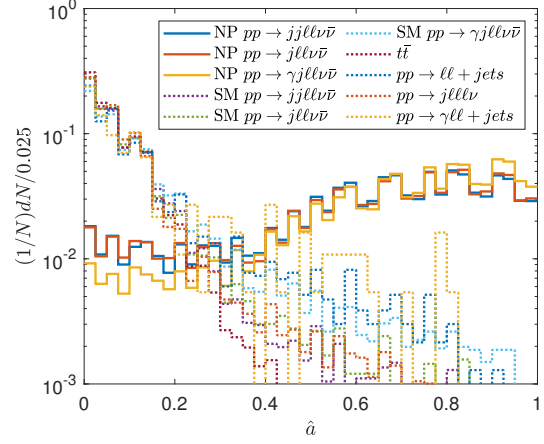
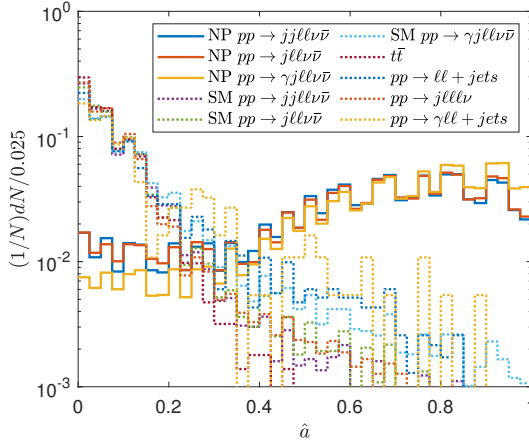
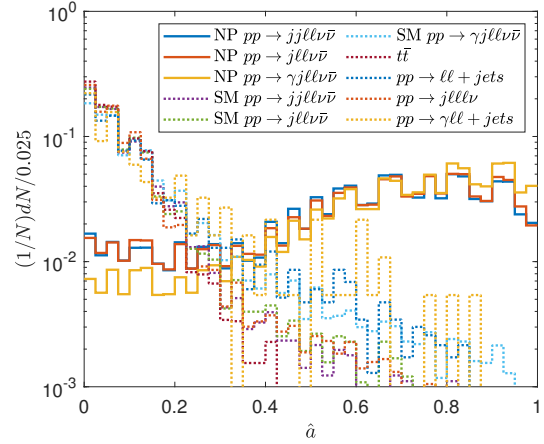
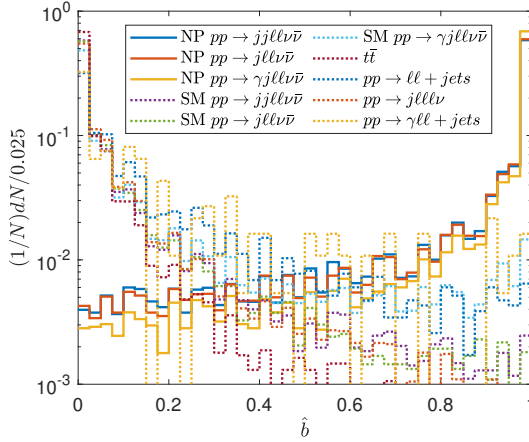
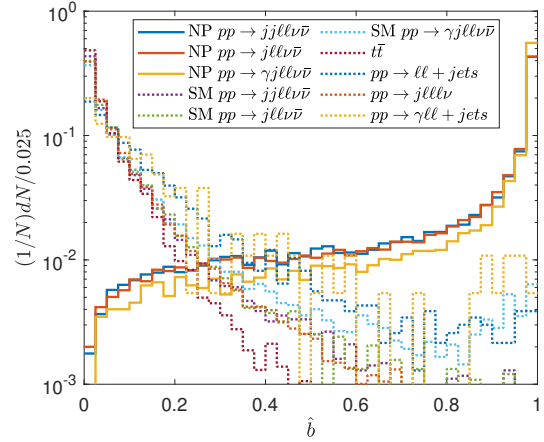
(b) VQSN with  $l = 5$ (c) VQSN with  $l = 10$ (d) VQSN with  $l = 15$ (e) t-KNN with  $k = 100$ (f) t-KNN with  $k = 1000$ 

FIG. 10. The normalized distributions of  $\hat{a}$  and  $\hat{b}$  for different processes using different event selection strategies. For t-KNN, only the cases of  $k = 100$  and  $1000$  are shown as examples.

set), respectively. The normalized distributions of  $\hat{a}$  and  $\hat{b}$  for the validation set are shown in Fig. 10. It can be seen that, for both VQSN and t-KNN event selection strategies,  $\hat{a}$  and  $\hat{b}$  can be used for discriminate the signal events from background events. The distributions of  $\hat{a}$  for the VQSN shows that the difference from different  $ls$  is small. Furthermore, the  $\hat{a}$  of a background event is more closely aligned with 0 when using an ansatz.

When NP signals are not found, the constraints on the operator coefficients are of interest. The expected coefficient constraints can be estimated using Eq. (4) and the cross-section. When the interference term is considered, the total cross-section after cuts can be written as,

$$\begin{aligned} \sigma(f_0) = & \left( \sum_p \sigma_{\text{SM}}^{(p)} + \sigma_{t\bar{t}} \varepsilon_b^2 Br_{W \rightarrow \ell\nu}^2 \varepsilon_{N_{part}}^{t\bar{t}} \varepsilon_{t\bar{t}} + \tilde{\sigma}_{bg} \right) \\ & + f_0 \sum_p \sigma_{\text{int}}^{(p)} + f_0^2 \sum_p \sigma_{\text{NP}}^{(p)}, \end{aligned} \quad (7)$$

where the summation  $\sum_p$  is over the three processes  $pp \rightarrow jj\ell^+\ell^-\nu\bar{\nu}$ ,  $pp \rightarrow j\ell^+\ell^-\nu\bar{\nu}$  and  $pp \rightarrow \gamma j\ell^+\ell^-\nu\bar{\nu}$ ,  $\sigma_{t\bar{t}}$  is the inclusive cross-section of the production of  $t\bar{t} + jets$  which is taken as 832 (pb),  $\varepsilon_b = 1 - 77\%$  is from mis-tagging of  $b$ -jets,  $Br_{W \rightarrow \ell\nu} = 21.7\%$  [88],  $\varepsilon_{N_{part}}^{t\bar{t}}$  is the cut efficiency of  $N_{part}$  cut in Table VI,  $\varepsilon_{t\bar{t}}$  is the cut efficiency of (V)QSN and (t-)KNN estimated using the  $t\bar{t}$  events, and  $\tilde{\sigma}_{bg}$  is the sum of  $\ell\ell + jets$ ,  $j\ell\ell\ell\nu$ , and  $\gamma\ell\ell + jets$  backgrounds after all cuts. Then,  $\sigma_{bg} = \sigma(f_0 = 0)$  and  $\sigma_s = \sigma(f_0) - \sigma_{bg}$ ,

To consider the interference, we scanned the interval  $f_0 \in [-0.2 \text{ TeV}^{-4}, 0.2 \text{ TeV}^{-4}]$ . For a given  $\hat{a}_{th}$  (or  $\hat{b}_{th}$ ) and a given  $f_0$ , one can obtain the cross-section  $\sigma^{(p)}(f_0)$  after cuts as well as  $\varepsilon_{t\bar{t}}$  and  $\tilde{\sigma}_{bg}$ , then  $\sigma(f_0)$  and  $\mathcal{S}_{stat}$  can be obtained. The tunable parameters  $\hat{a}_{th}$  and  $\hat{b}_{th}$  are chosen to maximize  $\mathcal{S}_{stat}$  when  $f_0 = 0.2 \text{ TeV}^{-4}$ . The optimal  $\hat{a}_{th}$ ,  $\hat{b}_{th}$ , as well as  $\varepsilon_{t\bar{t}}$  and  $\tilde{\sigma}_{bg}$  at this point are listed in Table VII.  $\sigma(f_0)$  with different  $f_0$  can be fitted according to Eq. (7). The fittings of  $\sigma(f_0)$  at the optimal  $\hat{a}_{th}$  and  $\hat{b}_{th}$  are shown in Fig. 11. It can be seen that the bilinear function fits well. In the region of coefficient in consideration, the interference is relatively small, and is found to be positive.

When the fittings of  $\sigma(f_0)$  are obtained, the expected constraints at  $\mathcal{S}_{stat} = 2, 3$  and 5 can be solved. The results at the 13 TeV LHC with  $L = 137 \text{ fb}^{-1}$  are listed in Table VIII. The results indicate that the expected coefficient constraints of the various algorithms are generally at a same order of magnitude. It is evident that the constraints obtained by VQSN are more off-centered, indicating that the contribution of the interference terms is

			$\sigma_{t\bar{t}}$ (fb)	$\varepsilon_{t\bar{t}}$	$\tilde{\sigma}_{bg}$ (fb)
QSN		$\hat{a}_{th}$ 0.56	0.0277	$2.74 \times 10^{-4}$	1.58
VQSN	$l$	$\hat{a}_{th}$			
	5	0.81	0.00498	$4.92 \times 10^{-5}$	0.195
	10	0.88	0.00213	$2.11 \times 10^{-5}$	0.0135
	15	0.9	0.00213	$2.11 \times 10^{-5}$	$1.97 \times 10^{-4}$
KNN	$k$				
	1		0.322	$3.19 \times 10^{-3}$	7.52
	10		0.133	$1.32 \times 10^{-3}$	4.61
	100		0.119	$1.18 \times 10^{-3}$	4.35
	1000		0.0547	$5.42 \times 10^{-4}$	2.92
t-KNN	$k$	$\hat{b}_{th}$			
	10	0.9	0.0163	$1.62 \times 10^{-4}$	0.880
	100	0.99	0.000711	$7.03 \times 10^{-6}$	0.0583
	1000	0.998	0.000711	$7.03 \times 10^{-6}$	$2.34 \times 10^{-5}$

TABLE VII. The cross-sections after the (V)QSN and (t-)KNN event selection strategies for the  $t\bar{t}$  process ( $\sigma_{t\bar{t}}$ ) as well as the  $ll + jets$ ,  $jlll\nu$  and  $\gamma ll + jets$  backgrounds ( $\tilde{\sigma}_{bg}$ ). The cut efficiencies of the (V)QSN and (t-)KNN event selection strategies for the  $t\bar{t}$  process ( $\sigma_{t\bar{t}}$ ) are listed. The optimal  $\hat{a}_{th}$  and  $\hat{b}_{th}$  for VQSN and t-KNN are also listed.

more preserved. This may confer an advantage to VQSN when the coefficient is in a more stringent region as the luminosity increases.

Using the upper bound of coefficient constraint, one can set a constraint on  $M_0$  when  $f_0$  is positive. The results at  $\mathcal{S}_{stat} = 2$  are shown in Fig. 12, which provides a more clear comparison of different algorithms. It can be seen that t-KNN ( $k = 1000$ ) is the most effective, followed by t-KNN ( $k = 100$ ), VQSN ( $l = 15$ ), and VQSN ( $l = 10$ ). Furthermore, the result presented in Ref. [91] ( $M_0 \geq 1040$  MeV) are shown as a dashed line, and the four aforementioned cases demonstrate tighter constraints. This suggests that the processes under consideration are sensitive to the gQGCs and are worth of consideration in the global

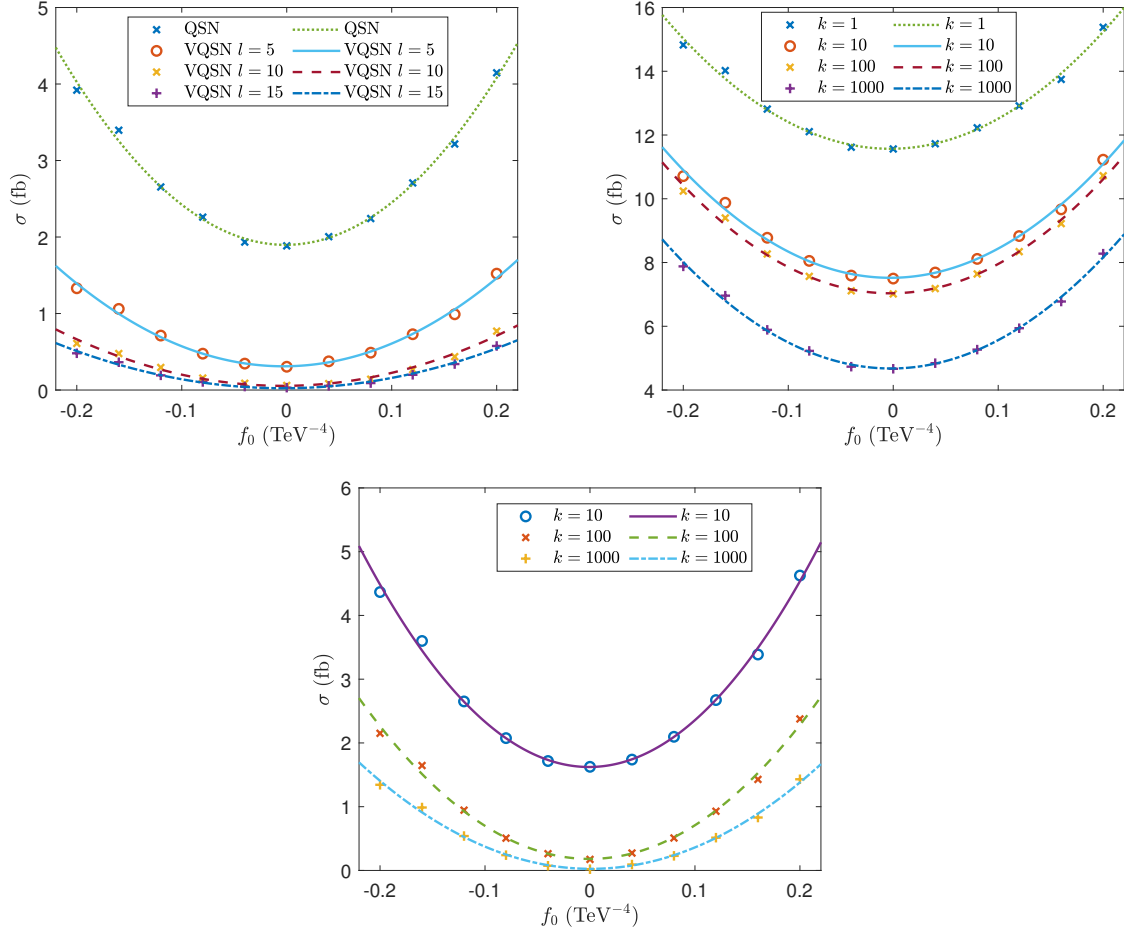


FIG. 11. The total cross-sections  $\sigma(f_0)$  after the (V)QSN and (t-)KNN event selection strategies at different  $f_0$ , as well as the fitted total cross-sections. The cases of (V)QSN are shown in the left panel, the cases of KNN are shown in the middle panel, and the cases of t-KNN are shown in the right panel, respectively.

fit of the constraints on gQGCs. Furthermore, the results demonstrate the efficacy of the t-KNN and VQSN algorithms employed. The validity is a crucial consideration when using an EFT [133–144], and can usually be tested through unitarity. According to the Ref. [91], the region of coefficients in this study is free from the violation of unitarity.

We use the average success rate of background events to estimate the cc necessary to determine the classification of one vector when  $c' = 100$ . The requisite number of quantum gates is presented in Table IX. When counting the number of quantum gates, the single qubit gates are combined as the single-qubit unitary gates (denoted as  $U$ ), and the gates

		$\mathcal{S}_{stat}$		
		2	3	5
QSN		[-0.068, 0.065]	[-0.083, 0.081]	[-0.108, 0.106]
VQSN	$l$			
	5	[-0.063, 0.057]	[-0.077, 0.071]	[-0.101, 0.095]
	10	[-0.057, 0.049]	[-0.070, 0.063]	[-0.094, 0.086]
	15	[-0.053, 0.046]	[-0.066, 0.059]	[-0.089, 0.082]
KNN	$k$			
	1	[-0.084, 0.078]	[-0.102, 0.097]	[-0.132, 0.126]
	10	[-0.076, 0.071]	[-0.093, 0.088]	[-0.120, 0.115]
	100	[-0.075, 0.070]	[-0.092, 0.086]	[-0.118, 0.113]
	1000	[-0.068, 0.064]	[-0.084, 0.079]	[-0.108, 0.104]
t-KNN	$k$			
	10	[-0.056, 0.055]	[-0.069, 0.067]	[-0.090, 0.088]
	100	[-0.039, 0.038]	[-0.048, 0.047]	[-0.064, 0.063]
	1000	[-0.031, 0.031]	[-0.039, 0.039]	[-0.053, 0.053]

TABLE VIII. The expected constraints on the  $f_0$  ( $\text{TeV}^{-4}$ ) at  $\sqrt{s} = 13$  TeV,  $L = 137$  fb $^{-1}$  and  $\mathcal{S}_{stat} = 2, 3,$  and  $5$  using different event selection strategies.

irrelevant of the measurements are removed. The total number of quantum gates is defined as the sum of the number of  $U$  gates and the number of two-qubit gates. It can be observed that the cc for VQSN is less than that of (t-)KNN. This indicates that even with classical data, VQSN can still be more efficient than (t-)KNN. Furthermore, the cc is reduced by an order of magnitude when  $l = 5$ . Note that, the superiority of VQSN can be even further evident for a larger training dataset or a larger  $d$ .

Meanwhile, the depth of the quantum circuit is also a significant metric. Given the noise in quantum computers at this stage, the depth of a quantum circuit is limited. In addition, since quantum gates on different qubits can act in parallel, the depth is a measure of time complexity. For VQSN, the depth of the circuit when a SCA entanglement layer is employed is less than or equal to  $dep_{ans} + dep_{ae}$  with  $dep_{ans} = (n_q + 1)l + 1$  and  $dep_{ae} = 4d - 3 - 4 \log_2(d)$  are the depths of the ansatz and inverse of amplitude encode, respectively. It can be seen that

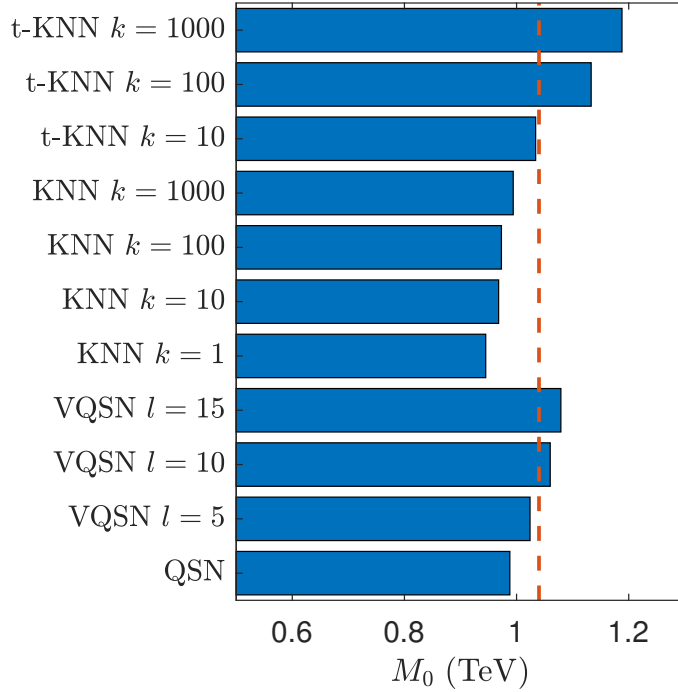


FIG. 12. Comparison of the constraints on  $M_0$  when  $f_0$  is positive at  $\mathcal{S}_{stat} = 2$  obtained from different event selection strategies. The result of Ref. [91] is shown as the dashed line.

	QSN	VQSN			(t-)KNN
$l$		5	10	15	
$R_y$	458759	121	216	311	
$R_z$	458759	121	216	311	
$U$	914865	106	201	296	
CZ	0	95	190	285	
CNOT	917506	8	8	8	
total	1832371	209	399	589	
cc	$9.9 \times 10^8$	$8.5 \times 10^4$	$1.6 \times 10^5$	$2.4 \times 10^5$	$8.5 \times 10^5$
depth	1832354	105	210	315	

TABLE IX. The number of single qubit gates, two qubit gates used in (V)QSN event selection strategies. The ‘total’ represents the number of gates to measure the classification assignment once for one test vector. The depths of circuits are also listed.

the SCA entanglement layer introduces much more depth than the pairwise entanglement layer. Due to the large amount of test data with interference between the SM and NP, which would consume too much machine time, we only performed the simulation of quantum computation on a simulator, so we choose the better-fitting SCA instead of pairwise in this subsection.

### E. Search for the anomalies quartic gauge couplings in the tri-photon process at muon colliders

#### 1. The contribution of the anomalies quartic gauge couplings in the tri-photon process

As machine learning algorithms, (V)QSN and (t-)KNN should not depend on the NP or process to be searched. Thus, as an example, we consider the dimension-8 operators contributing to the anomalies quartic gauge couplings (aQGCs) in the tri-photon process at muon colliders. Due to the attention paid to vector boson scattering (VBS) processes at the LHC, the aQGCs which are suitable to be studied in VBS processes have also been widely studied phenomenologically [96, 100, 102, 103, 145] and experimentally [104–113, 146–150].

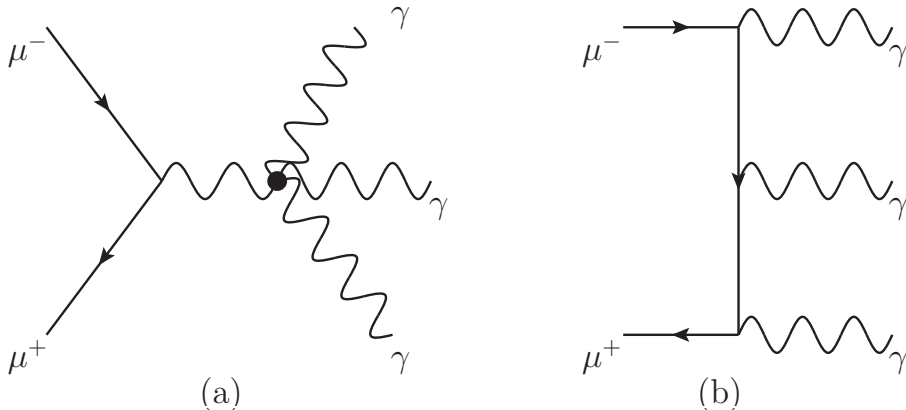


FIG. 13. Feynman diagrams the tri-photon process. There are two diagrams of aQGCs shown in (a) where the s-channel propagator can be either  $Z$  or  $\gamma$ . There are six diagrams in the SM, one of which is shown in (b) and other five diagrams can be obtained by permuting the photons in the final state.

The dimension-8 operators contributing to the aQGCs are often classified as scalar/longitudinal

operators  $O_{S_i}$ , mixed transverse and longitudinal operators  $O_{M_i}$  and transverse operators  $O_{T_i}$ . It has been found that the tri-photon processes at the muon colliders are sensitive to the  $O_{T_i}$  operators [151], they are [100, 152, 153],

$$\begin{aligned}
O_{T,0} &= \text{Tr} \left[ \widehat{W}_{\mu\nu} \widehat{W}^{\mu\nu} \right] \times \text{Tr} \left[ \widehat{W}_{\alpha\beta} \widehat{W}^{\alpha\beta} \right], \\
O_{T,1} &= \text{Tr} \left[ \widehat{W}_{\alpha\nu} \widehat{W}^{\mu\beta} \right] \times \text{Tr} \left[ \widehat{W}_{\mu\beta} \widehat{W}^{\alpha\nu} \right], \\
O_{T,2} &= \text{Tr} \left[ \widehat{W}_{\alpha\mu} \widehat{W}^{\mu\beta} \right] \times \text{Tr} \left[ \widehat{W}_{\beta\nu} \widehat{W}^{\nu\alpha} \right], \\
O_{T,5} &= \text{Tr} \left[ \widehat{W}_{\mu\nu} \widehat{W}^{\mu\nu} \right] \times B_{\alpha\beta} B^{\alpha\beta}, \\
O_{T,6} &= \text{Tr} \left[ \widehat{W}_{\alpha\nu} \widehat{W}^{\mu\beta} \right] \times B_{\mu\beta} B^{\alpha\nu}, \\
O_{T,7} &= \text{Tr} \left[ \widehat{W}_{\alpha\mu} \widehat{W}^{\mu\beta} \right] \times B_{\beta\nu} B^{\nu\alpha}, \\
O_{T,8} &= B_{\mu\nu} B^{\mu\nu} \times B_{\alpha\beta} B^{\alpha\beta}, \\
O_{T,9} &= B_{\alpha\mu} B^{\mu\beta} \times B_{\beta\nu} B^{\nu\alpha},
\end{aligned} \tag{8}$$

where  $\widehat{W} \equiv \vec{\sigma} \cdot \vec{W}/2$  with  $\sigma$  being the Pauli matrices and  $\vec{W} = \{W^1, W^2, W^3\}$ ,  $B_\mu$  and  $W_\mu^i$  are  $U(1)_Y$  and  $SU(2)_I$  gauge fields, and  $B_{\mu\nu}$  and  $W_{\mu\nu}$  correspond to the field strength tensors. The Feynman diagrams are shown in Fig. 13. The contribution of  $O_{T,1}$  and  $O_{T,6}$  operator are as same as the ones of  $O_{T,0}$  and  $O_{T,5}$ , respectively, therefore are not studied.

## 2. Training of the ansatz

	$v^0$	$v^1$	$v^2$	$v^3$	$v^4$	$v^5$
observables	$E_{\gamma_1}$	$p_{\gamma_1}^T$	$E_{\gamma_2}$	$p_{\gamma_2}^T$	$E_{\gamma_3}$	$p_{\gamma_3}^T$

TABLE X. Same as Table I but for the tri-photon processes at the muon colliders.

Different from the previous subsections, in the generation of the events, the standard cuts are set to be as same as the default except for the  $p_\gamma^T$  cut which is set to be  $p_\gamma^T \geq 0.1 E_{beam}$  where  $E_{beam}$  is the beam energy which can suppressing the SM background and ease the pressure on numerical computation consumption. The cases of  $\sqrt{s} = 3$  TeV, 10 TeV, 14 TeV and 30 TeV are considered [125, 126]. To generate the training set,  $2^{16} + 2^{16}$  events are chosen from the SM background and the NP events. It has been shown that, the kinematic features are similar for different operators, therefore in the training set, we use only the events from

$O_{T_0}$ . It is required that the final state to have at least three photons. The observables chosen to form the feature space are listed in Table X, where  $E_{\gamma_{1,2,3}}$  and  $p_{\gamma_{1,2,3}}^T$  are energies and transverse momenta of the hardest, second hardest and the third hardest photons. Using this feature space,  $d = 6$  and  $d' = 4$ , and with  $2^{17}$  events, the ansatz takes  $n_q = 19$  qubits. In this subsection, we also use the SCA entanglement layer and with  $l = 10$ , the circuit is the one shown in Fig. 1. (d). After training, the fidelities are 46.8%, 46.8%, 46.9% and 46.9% for the cases of  $\sqrt{s} = 3$  TeV, 10 TeV, 14 TeV and 30 TeV, respectively.

### 3. Numerical results

$\sqrt{s}$	3 TeV	10 TeV	14 TeV	30 TeV
$ f_{T_0}/\Lambda^4 $	$\leq 0.3$	$\leq 0.0015$	$\leq 0.0005$	$\leq 0.00005$
$ f_{T_2}/\Lambda^4 $	$\leq 0.5$	$\leq 0.002$	$\leq 0.0008$	$\leq 0.00008$
$ f_{T_5}/\Lambda^4 $	$\leq 0.06$	$\leq 0.0003$	$\leq 0.0001$	$\leq 0.000008$
$ f_{T_7}/\Lambda^4 $	$\leq 0.1$	$\leq 0.0005$	$\leq 0.00015$	$\leq 0.000015$
$ f_{T_8}\Lambda^4 $	$\leq 0.01$	$\leq 0.00005$	$\leq 0.000015$	$\leq 0.0000015$
$ f_{T_9}/\Lambda^4 $	$\leq 0.016$	$\leq 0.00008$	$\leq 0.00002$	$\leq 0.000002$

TABLE XI. The ranges of operator coefficients used in the scanning ( $\text{TeV}^{-4}$ ).

The test data are generated with the interference between the SM and NP considered and with one operator at a time. We scan the parameters with the coefficients in the regions listed in Table XI. After the events are generated,  $10^5$  events are picked at each coefficient after the requirement of at least three photons in the final states. The cross-section after cut can be written as,

$$\sigma(f_{T_i}) = \sigma_{\text{SM}} + f_{T_i}\sigma_{\text{int}} + f_{T_i}^2\sigma_{\text{NP}}, \quad (9)$$

where  $\sigma_{\text{SM}}$ ,  $\sigma_{\text{int}}$  and  $\sigma_{\text{NP}}$  are parameters to be fitted representing the SM, interference and NP contributions. In this subsection, we use a fixed  $c' = 200$ , choosing  $\hat{a}_{th} = 0.35$  for the cases of  $\sqrt{s} = 3$  TeV, 10 TeV and 14 TeV, and  $\hat{a}_{th} = 0.36$  for the case of  $\sqrt{s} = 30$  TeV, the cross-sections after cut and the fitted cross-sections are shown in Fig. 14.

Using the designed luminosities for both the ‘‘conservative’’ and ‘‘optimistic’’ cases [125, 126] and the fitted cross-sections, the expected constraints can be estimated using Eq. (4).

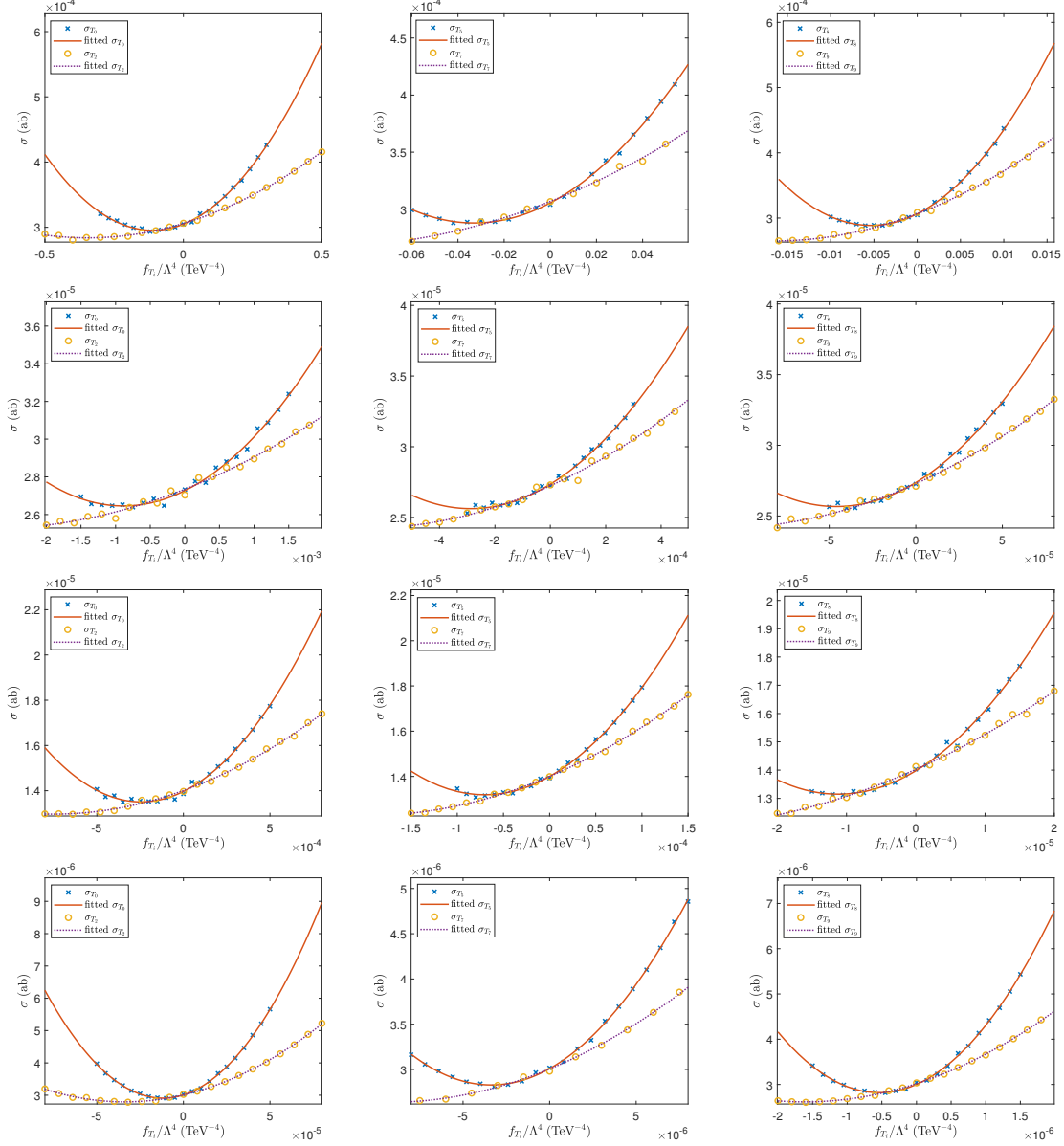


FIG. 14. The cross-sections  $\sigma$  after cuts compared with the fitted  $\sigma$  according to Eq. (9) of  $f_{T_i}/\Lambda^4$  at different collision energies,  $\sqrt{s} = 3$  TeV (row 1), 10 TeV (row 2), 14 TeV (row 3), and 30 TeV (row 4).

The results are listed in Tables XII and XIII. It can be shown that the VQSN is effective in the search for aQGCs, the expected constraints generally outperform the ones obtained by a traditional event selection strategy [151].

In the case of  $l = 10$ , the number of  $U$  gates is 64 and the number of  $CZ$  gates is 62, the  $cc$  is estimated by average  $r$  of the entire test dataset and  $c' = 200$  that  $c'/r = 564$ , so the

	$\mathcal{S}_{stat}$	3 TeV 1 ab <sup>-1</sup> (10 <sup>-2</sup> TeV <sup>-4</sup> )	10 TeV 10 ab <sup>-1</sup> (10 <sup>-4</sup> TeV <sup>-4</sup> )	14 TeV 10 ab <sup>-1</sup> (10 <sup>-4</sup> TeV <sup>-4</sup> )	30 TeV 10 ab <sup>-1</sup> (10 <sup>-5</sup> TeV <sup>-4</sup> )
$f_{T_0}(f_{T_1})/\Lambda^4$	2	[-35.30, 13.12]	[-29.03, 11.28]	[-8.54, 3.67]	[-5.38, 3.01]
	3	[-39.79, 17.62]	[-32.85, 15.10]	[-9.76, 4.89]	[-6.31, 3.95]
	5	[-47.31, 25.14]	[-39.22, 21.47]	[-11.79, 6.92]	[-7.90, 5.53]
$f_{T_2}/\Lambda^4$	2	[-90.53, 21.33]	[-75.97, 17.78]	[-21.26, 6.21]	[-12.00, 5.22]
	3	[-98.78, 29.59]	[-82.88, 24.69]	[-23.57, 8.53]	[-13.78, 7.00]
	5	[-113.06, 43.87]	[-94.83, 36.64]	[-27.52, 12.48]	[-16.83, 10.04]
$f_{T_5}(f_{T_6})/\Lambda^4$	2	[-9.04, 2.44]	[-7.81, 2.07]	[-2.11, 0.70]	[-1.26, 0.58]
	3	[-9.95, 3.35]	[-8.59, 2.84]	[-2.36, 0.96]	[-1.45, 0.78]
	5	[-11.51, 4.92]	[-9.93, 4.18]	[-2.79, 1.38]	[-1.78, 1.11]
$f_{T_7}/\Lambda^4$	2	[-23.68, 3.76]	[-16.59, 3.08]	[-5.08, 1.10]	[-2.84, 0.97]
	3	[-25.26, 5.34]	[-17.85, 4.33]	[-5.52, 1.53]	[-3.20, 1.33]
	5	[-28.07, 8.15]	[-20.06, 6.54]	[-6.28, 2.30]	[-3.82, 1.95]
$f_{T_8}/\Lambda^4$	2	[-1.46, 0.39]	[-1.25, 0.33]	[-0.33, 0.11]	[-0.20, 0.09]
	3	[-1.61, 0.54]	[-1.38, 0.46]	[-0.37, 0.15]	[-0.23, 0.12]
	5	[-1.86, 0.79]	[-1.59, 0.68]	[-0.44, 0.22]	[-0.28, 0.18]
$f_{T_9}/\Lambda^4$	2	[-3.92, 0.60]	[-2.78, 0.50]	[-0.94, 0.18]	[-0.48, 0.16]
	3	[-4.17, 0.85]	[-2.99, 0.71]	[-1.01, 0.25]	[-0.54, 0.22]
	5	[-4.63, 1.31]	[-3.35, 1.07]	[-1.14, 0.38]	[-0.64, 0.32]

TABLE XII. In the ‘‘conservative’’ case, the projected sensitivities on the coefficients of the  $O_{T_i}$  operators at the muon colliders for various c.m. energies and integrated luminosities.

cc is  $7.4 \times 10^4$  for one test event. If the (t-)KNN is used, the cc is  $2^{17}d' = 7.86 \times 10^5$  for one test event, therefore the cc of VQSN is one order of magnitude smaller.

#### IV. SUMMARY

In this study, we present a novel (V)QSN algorithm for classification that is designed to operate on a quantum computer. A numerical example running on the *tianyan176-2* of the

	$\mathcal{S}_{stat}$	14 TeV 20 ab <sup>-1</sup> (10 <sup>-5</sup> TeV <sup>-4</sup> )	30 TeV 90 ab <sup>-1</sup> (10 <sup>-6</sup> TeV <sup>-4</sup> )
$f_{T_0}(f_{T_1})/\Lambda^4$	2	[-77.26, 28.50]	[-37.51, 13.86]
	3	[-87.06, 38.30]	[-42.27, 18.63]
	5	[-103.48, 54.72]	[-50.26, 26.61]
$f_{T_2}/\Lambda^4$	2	[-197.39, 46.98]	[-90.17, 22.29]
	3	[-215.55, 65.15]	[-98.72, 30.84]
	5	[-246.95, 96.54]	[-113.45, 45.58]
$f_{T_5}(f_{T_6})/\Lambda^4$	2	[-19.41, 5.37]	[-9.28, 2.53]
	3	[-21.41, 7.37]	[-10.23, 3.48]
	5	[-24.83, 10.79]	[-11.85, 5.11]
$f_{T_7}/\Lambda^4$	2	[-47.96, 8.15]	[-22.65, 3.91]
	3	[-51.34, 11.52]	[-24.27, 5.52]
	5	[-57.33, 17.52]	[-27.13, 8.39]
$f_{T_8}/\Lambda^4$	2	[-3.08, 0.84]	[-1.48, 0.40]
	3	[-3.39, 1.15]	[-1.63, 0.55]
	5	[-3.93, 1.69]	[-1.89, 0.81]
$f_{T_9}/\Lambda^4$	2	[-8.92, 1.33]	[-3.86, 0.63]
	3	[-9.49, 1.89]	[-4.13, 0.89]
	5	[-10.50, 2.90]	[-4.60, 1.36]

TABLE XIII. Same as Table XII but for the “optimistic” case.

*Tianyan quantum computing cloud platform* is established to show that the VQSN is suitable for a general proposed classification. This algorithm is analogous to the KNN algorithm. We employ the (V)QSN and the (t-)KNN with the objective of identifying signals of NP in different processes.

The VQSN is used in the phenomenological study of the gQGCs in the process  $\mu^+\mu^- \rightarrow jj\nu\bar{\nu}$  at a  $\sqrt{s} = 3$  TeV muon collider. The VQSN event selection strategy is tested on the *tianyan176-2*. The expected coefficient constraints are obtained and found to be at the same order of magnitude as the traditional event selection strategy in Ref. [124], indicating that

the VQSN is an effective method and possesses noise tolerance.

The gQGCs at the LHC are also studied, using the processes  $pp \rightarrow jj\ell^+\ell^-\nu\bar{\nu}$ ,  $pp \rightarrow j\ell^+\ell^-\nu\bar{\nu}$  and  $pp \rightarrow \gamma j\ell^+\ell^-\nu\bar{\nu}$ . These processes can be concluded to be sensitive to the gQGCs. The constraints on the coefficient are of a similar magnitude to those obtained in the  $pp \rightarrow \gamma\gamma$  process [91]. Consequently, they can serve as a valuable supplement to the constraints on the gQGCs. Moreover, the  $pp \rightarrow jj\ell^+\ell^-\nu\bar{\nu}$  process contains a VBS process which is expected to be more significant at higher energies [151], therefore is expected to be more important at future colliders such as the HE-LHC and FCC-hh [154, 155].

Another application is the contribution of the aQGCs in the tri-photon processes at muon colliders. In this case, only the VQSN is studied. The expected constraints are obtained, and found to be more strengthen than the ones obtained using an traditional event selection strategy [151].

In terms of cc, the VQSN is capable of achieving the same order of magnitude of the discriminative power to that of the KNN, while requiring one order of magnitude less cc in the three applications. It is important to note that the datasets used in this study are classical, i.e., even when working with classical data, the VQSN can demonstrate its superiority in efficiency. When keeping the amount of test data much larger than the amount of training data, the larger training dataset and the larger feature space, the more efficient the VQSN is, the significance of VQSN is likely to increase as the processes under consideration become more intricate.

This study has not addressed further improvements in encoding the datasets in optimistic ways [86, 87] which are suitable for cooperation with (V)QSN. Furthermore, it would be beneficial to investigate the simulation of the collision process on a quantum computer. Reading results directly from a quantum computer is resource intensive, QSN can process data within the quantum computer, avoiding this consumption. In particular, it is plausible that the training dataset originates from simulations on a quantum computer, while the test dataset is derived from classical data obtained from a collider. This scenario is well-suited to the QSN.

In conclusion, QSN and VQSN are suitable for the NP phenomenological study.

## ACKNOWLEDGMENTS

We sincerely thank the *Tianyan quantum computing cloud platform* of China Telecom Quantum Information Technology Group Co., LTD. for providing quantum computer machine time and technical support. This work was supported in part by the National Natural Science Foundation of China under Grants Nos. 11875157 and 12147214, and the Natural Science Foundation of the Liaoning Scientific Committee No. LJKZ0978.

- 
- [1] Y. Farzan and M. Tortola, Neutrino oscillations and Non-Standard Interactions, [Front. in Phys.](#) **6**, 10 (2018), [arXiv:1710.09360 \[hep-ph\]](#).
  - [2] *Neutrino Non-Standard Interactions: A Status Report*, Vol. 2 (2019) [arXiv:1907.00991 \[hep-ph\]](#).
  - [3] C. A. Argüelles *et al.*, Snowmass white paper: beyond the standard model effects on neutrino flavor: Submitted to the proceedings of the US community study on the future of particle physics (Snowmass 2021), [Eur. Phys. J. C](#) **83**, 15 (2023), [arXiv:2203.10811 \[hep-ph\]](#).
  - [4] T. Aaltonen *et al.* (CDF), High-precision measurement of the  $W$  boson mass with the CDF II detector, [Science](#) **376**, 170 (2022).
  - [5] J. de Blas, M. Pierini, L. Reina, and L. Silvestrini, Impact of the Recent Measurements of the Top-Quark and W-Boson Masses on Electroweak Precision Fits, [Phys. Rev. Lett.](#) **129**, 271801 (2022), [arXiv:2204.04204 \[hep-ph\]](#).
  - [6] B. Abi *et al.* (Muon g-2), Measurement of the Positive Muon Anomalous Magnetic Moment to 0.46 ppm, [Phys. Rev. Lett.](#) **126**, 141801 (2021), [arXiv:2104.03281 \[hep-ex\]](#).
  - [7] D. P. Aguillard *et al.* (Muon g-2), Measurement of the Positive Muon Anomalous Magnetic Moment to 0.20 ppm, [Phys. Rev. Lett.](#) **131**, 161802 (2023), [arXiv:2308.06230 \[hep-ex\]](#).
  - [8] T. Aoyama *et al.*, The anomalous magnetic moment of the muon in the Standard Model, [Phys. Rept.](#) **887**, 1 (2020), [arXiv:2006.04822 \[hep-ph\]](#).
  - [9] A. Crivellin and B. Mellado, Anomalies in Particle Physics (2023) [arXiv:2309.03870 \[hep-ph\]](#).
  - [10] J. Ellis, Outstanding questions: Physics beyond the Standard Model, [Phil. Trans. Roy. Soc. Lond. A](#) **370**, 818 (2012).
  - [11] V. Innocente, Y. F. Wang, and Z. P. Zhang, Identification of tau decays using a neural

- network, *Nucl. Instrum. Meth. A* **323**, 647 (1992).
- [12] K. Albertsson *et al.*, Machine Learning in High Energy Physics Community White Paper, *J. Phys. Conf. Ser.* **1085**, 022008 (2018), [arXiv:1807.02876 \[physics.comp-ph\]](#).
- [13] D. Guest, K. Cranmer, and D. Whiteson, Deep Learning and its Application to LHC Physics, *Ann. Rev. Nucl. Part. Sci.* **68**, 161 (2018), [arXiv:1806.11484 \[hep-ex\]](#).
- [14] A. Radovic, M. Williams, D. Rousseau, M. Kagan, D. Bonacorsi, A. Himmel, A. Aurisano, K. Terao, and T. Wongjirad, Machine learning at the energy and intensity frontiers of particle physics, *Nature* **560**, 41 (2018).
- [15] P. Baldi, P. Sadowski, and D. Whiteson, Searching for Exotic Particles in High-Energy Physics with Deep Learning, *Nature Commun.* **5**, 4308 (2014), [arXiv:1402.4735 \[hep-ph\]](#).
- [16] J. Ren, L. Wu, J. M. Yang, and J. Zhao, Exploring supersymmetry with machine learning, *Nucl. Phys. B* **943**, 114613 (2019), [arXiv:1708.06615 \[hep-ph\]](#).
- [17] M. Abdughani, J. Ren, L. Wu, and J. M. Yang, Probing stop pair production at the LHC with graph neural networks, *JHEP* **08**, 055, [arXiv:1807.09088 \[hep-ph\]](#).
- [18] J. Ren, L. Wu, and J. M. Yang, Unveiling CP property of top-Higgs coupling with graph neural networks at the LHC, *Phys. Lett. B* **802**, 135198 (2020), [arXiv:1901.05627 \[hep-ph\]](#).
- [19] M. Letizia, G. Losapio, M. Rando, G. Grosso, A. Wulzer, M. Pierini, M. Zanetti, and L. Rosasco, Learning new physics efficiently with nonparametric methods, *Eur. Phys. J. C* **82**, 879 (2022), [arXiv:2204.02317 \[hep-ph\]](#).
- [20] R. T. D’Agnolo, G. Grosso, M. Pierini, A. Wulzer, and M. Zanetti, Learning multivariate new physics, *Eur. Phys. J. C* **81**, 89 (2021), [arXiv:1912.12155 \[hep-ph\]](#).
- [21] R. T. D’Agnolo and A. Wulzer, Learning New Physics from a Machine, *Phys. Rev. D* **99**, 015014 (2019), [arXiv:1806.02350 \[hep-ph\]](#).
- [22] A. De Simone and T. Jacques, Guiding New Physics Searches with Unsupervised Learning, *Eur. Phys. J. C* **79**, 289 (2019), [arXiv:1807.06038 \[hep-ph\]](#).
- [23] J. Lee, N. Chanon, A. Levin, J. Li, M. Lu, Q. Li, and Y. Mao, Polarization fraction measurement in same-sign WW scattering using deep learning, *Phys. Rev. D* **99**, 033004 (2019), [arXiv:1812.07591 \[hep-ph\]](#).
- [24] M. A. Md Ali, N. Badrud’din, H. Abdullah, and F. Kemi, Alternate methods for anomaly detection in high-energy physics via semi-supervised learning, *Int. J. Mod. Phys. A* **35**, 2050131 (2020).

- [25] E. Fol, R. Tomás, J. Coello de Portugal, and G. Franchetti, Detection of faulty beam position monitors using unsupervised learning, *Phys. Rev. Accel. Beams* **23**, 102805 (2020).
- [26] G. Kasieczka *et al.*, The LHC Olympics 2020 a community challenge for anomaly detection in high energy physics, *Rept. Prog. Phys.* **84**, 124201 (2021), [arXiv:2101.08320 \[hep-ph\]](#).
- [27] M. Crispim Romão, N. F. Castro, and R. Pedro, Finding New Physics without learning about it: Anomaly Detection as a tool for Searches at Colliders, *Eur. Phys. J. C* **81**, 27 (2021), [Erratum: *Eur.Phys.J.C* 81, 1020 (2021)], [arXiv:2006.05432 \[hep-ph\]](#).
- [28] M. van Beekveld, S. Caron, L. Hendriks, P. Jackson, A. Leinweber, S. Otten, R. Patrick, R. Ruiz De Austri, M. Santoni, and M. White, Combining outlier analysis algorithms to identify new physics at the LHC, *JHEP* **09**, 024, [arXiv:2010.07940 \[hep-ph\]](#).
- [29] M. Kuusela, T. Vatanen, E. Malmi, T. Raiko, T. Aaltonen, and Y. Nagai, Semi-Supervised Anomaly Detection - Towards Model-Independent Searches of New Physics, *J. Phys. Conf. Ser.* **368**, 012032 (2012), [arXiv:1112.3329 \[physics.data-an\]](#).
- [30] Z. Chen, K. J. Satzinger, J. Atalaya, A. N. Korotkov, A. Dunsworth, D. Sank, C. Quintana, M. McEwen, R. Barends, P. V. Klimov, S. Hong, C. Jones, A. Petukhov, D. Kafri, S. Demura, B. Burkett, C. Gidney, A. G. Fowler, A. Paler, H. Putterman, I. Aleiner, F. Arute, K. Arya, R. Babbush, J. C. Bardin, A. Bengtsson, A. Bourassa, M. Broughton, B. B. Buckley, D. A. Buell, N. Bushnell, B. Chiaro, R. Collins, W. Courtney, A. R. Derk, D. Eppens, C. Erickson, E. Farhi, B. Foxen, M. Giustina, A. Greene, J. A. Gross, M. P. Harrigan, S. D. Harrington, J. Hilton, A. Ho, T. Huang, W. J. Huggins, L. B. Ioffe, S. V. Isakov, E. Jeffrey, Z. Jiang, K. Kechedzhi, S. Kim, A. Kitaev, F. Kostritsa, D. Landhuis, P. Laptev, E. Lucero, O. Martin, J. R. McClean, T. McCourt, X. Mi, K. C. Miao, M. Mohseni, S. Montazeri, W. Mruczkiewicz, J. Mutus, O. Naaman, M. Neeley, C. Neill, M. Newman, M. Y. Niu, T. E. O'Brien, A. Opremcak, E. Ostby, B. Pató, N. Redd, P. Roushan, N. C. Rubin, V. Shvarts, D. Strain, M. Szalay, M. D. Trevithick, B. Villalonga, T. White, Z. J. Yao, P. Yeh, J. Yoo, A. Zalcman, H. Neven, S. Boixo, V. Smelyanskiy, Y. Chen, A. Megrant, and J. Kelly, Exponential suppression of bit or phase errors with cyclic error correction, *Nature* **595**, 383–387 (2021), [arXiv:2102.06132](#).
- [31] F. Arute *et al.*, Quantum supremacy using a programmable superconducting processor, *Nature* **574**, 505 (2019), [arXiv:1910.11333 \[quant-ph\]](#).
- [32] J. Preskill, Quantum Computing in the NISQ era and beyond, *Quantum* **2**, 79 (2018),

- [arXiv:1801.00862 \[quant-ph\]](#).
- [33] R. P. Feynman, Simulating physics with computers, *Int. J. Theor. Phys.* **21**, 467 (1982).
  - [34] A. Roggero and J. Carlson, Dynamic linear response quantum algorithm, *Phys. Rev. C* **100**, 034610 (2019), [arXiv:1804.01505 \[quant-ph\]](#).
  - [35] A. Roggero, A. C. Y. Li, J. Carlson, R. Gupta, and G. N. Perdue, Quantum Computing for Neutrino-Nucleus Scattering, *Phys. Rev. D* **101**, 074038 (2020), [arXiv:1911.06368 \[quant-ph\]](#).
  - [36] C. W. Bauer *et al.*, Quantum Simulation for High-Energy Physics, *PRX Quantum* **4**, 027001 (2023), [arXiv:2204.03381 \[quant-ph\]](#).
  - [37] M. Carena, H. Lamm, Y.-Y. Li, and W. Liu, Improved Hamiltonians for Quantum Simulations of Gauge Theories, *Phys. Rev. Lett.* **129**, 051601 (2022), [arXiv:2203.02823 \[hep-lat\]](#).
  - [38] E. J. Gustafson, H. Lamm, F. Lovelace, and D. Musk, Primitive quantum gates for an SU(2) discrete subgroup: Binary tetrahedral, *Phys. Rev. D* **106**, 114501 (2022), [arXiv:2208.12309 \[quant-ph\]](#).
  - [39] H. Lamm, Y.-Y. Li, J. Shu, Y.-L. Wang, and B. Xu, Block encodings of discrete subgroups on a quantum computer, *Phys. Rev. D* **110**, 054505 (2024), [arXiv:2405.12890 \[hep-lat\]](#).
  - [40] M. Carena, H. Lamm, Y.-Y. Li, and W. Liu, Quantum error thresholds for gauge-redundant digitizations of lattice field theories, *Phys. Rev. D* **110**, 054516 (2024), [arXiv:2402.16780 \[hep-lat\]](#).
  - [41] Y. Y. Atas, J. Zhang, R. Lewis, A. Jahanpour, J. F. Haase, and C. A. Muschik, SU(2) hadrons on a quantum computer via a variational approach, *Nature Commun.* **12**, 6499 (2021), [arXiv:2102.08920 \[quant-ph\]](#).
  - [42] Y.-Y. Li, M. O. Sajid, and J. Unmuth-Yockey, Lattice holography on a quantum computer, *Phys. Rev. D* **110**, 034507 (2024), [arXiv:2312.10544 \[hep-lat\]](#).
  - [43] X. Cui, Y. Shi, and J.-C. Yang, Circuit-based digital adiabatic quantum simulation and pseudoquantum simulation as new approaches to lattice gauge theory, *JHEP* **08**, 160, [arXiv:1910.08020 \[quant-ph\]](#).
  - [44] Y.-T. Zou, Y.-J. Bo, and J.-C. Yang, Optimize quantum simulation using a force-gradient integrator, *EPL* **135**, 10004 (2021), [arXiv:2103.05876 \[quant-ph\]](#).
  - [45] I. M. Georgescu, S. Ashhab, and F. Nori, Quantum Simulation, *Rev. Mod. Phys.* **86**, 153 (2014), [arXiv:1308.6253 \[quant-ph\]](#).
  - [46] H. Lamm, S. Lawrence, and Y. Yamauchi (NuQS), Parton physics on a quantum computer,

- [Phys. Rev. Res. \*\*2\*\*, 013272 \(2020\)](#), [arXiv:1908.10439 \[hep-lat\]](#).
- [47] T. Li, X. Guo, W. K. Lai, X. Liu, E. Wang, H. Xing, D.-B. Zhang, and S.-L. Zhu (QuNu), Partonic collinear structure by quantum computing, [Phys. Rev. D \*\*105\*\*, L111502 \(2022\)](#), [arXiv:2106.03865 \[hep-ph\]](#).
- [48] M. G. Echevarria, I. L. Egusquiza, E. Rico, and G. Schnell, Quantum simulation of light-front parton correlators, [Phys. Rev. D \*\*104\*\*, 014512 \(2021\)](#), [arXiv:2011.01275 \[quant-ph\]](#).
- [49] A. Pérez-Salinas, J. Cruz-Martinez, A. A. Alhajri, and S. Carrazza, Determining the proton content with a quantum computer, [Phys. Rev. D \*\*103\*\*, 034027 \(2021\)](#), [arXiv:2011.13934 \[hep-ph\]](#).
- [50] S. P. Jordan, K. S. M. Lee, and J. Preskill, Quantum Computation of Scattering in Scalar Quantum Field Theories, [Quant. Inf. Comput. \*\*14\*\*, 1014 \(2014\)](#), [arXiv:1112.4833 \[hep-th\]](#).
- [51] N. Mueller, A. Tarasov, and R. Venugopalan, Deeply inelastic scattering structure functions on a hybrid quantum computer, [Phys. Rev. D \*\*102\*\*, 016007 \(2020\)](#), [arXiv:1908.07051 \[hep-th\]](#).
- [52] Y. Zhu, W. Zhuang, C. Qian, Y. Ma, D. E. Liu, M. Ruan, and C. Zhou, A Novel Quantum Realization of Jet Clustering in High-Energy Physics Experiments (2024) [arXiv:2407.09056 \[quant-ph\]](#).
- [53] J. Biamonte, P. Wittek, N. Pancotti, P. Rebentrost, N. Wiebe, and S. Lloyd, Quantum machine learning, [Nature \*\*549\*\*, 195 \(2017\)](#), [arXiv:1611.09347 \[quant-ph\]](#).
- [54] M. Schuld, I. Sinayskiy, and F. Petruccione, An introduction to quantum machine learning, [Contemporary Physics \*\*56\*\*, 172 \(2015\)](#).
- [55] D. P. García, J. Cruz-Benito, and F. J. García-Peñalvo, Systematic Literature Review: Quantum Machine Learning and its applications (2022) [arXiv:2201.04093 \[quant-ph\]](#).
- [56] W. Guan, G. Perdue, A. Pesah, M. Schuld, K. Terashi, S. Vallecorsa, and J.-R. Vlimant, Quantum Machine Learning in High Energy Physics, [Mach. Learn. Sci. Tech. \*\*2\*\*, 011003 \(2021\)](#), [arXiv:2005.08582 \[quant-ph\]](#).
- [57] S. L. Wu *et al.*, Application of quantum machine learning using the quantum variational classifier method to high energy physics analysis at the LHC on IBM quantum computer simulator and hardware with 10 qubits, [J. Phys. G \*\*48\*\*, 125003 \(2021\)](#), [arXiv:2012.11560 \[quant-ph\]](#).
- [58] E. Grant, M. Benedetti, S. Cao, A. Hallam, J. Lockhart, V. Stojevic, A. G. Green, and S. Severini, Hierarchical quantum classifiers, [npj Quantum Inf. \*\*4\*\*, 65 \(2018\)](#).

- [59] K. Terashi, M. Kaneda, T. Kishimoto, M. Saito, R. Sawada, and J. Tanaka, Event Classification with Quantum Machine Learning in High-Energy Physics, *Comput. Softw. Big Sci.* **5**, 2 (2021), [arXiv:2002.09935 \[physics.comp-ph\]](#).
- [60] S. L. Wu *et al.*, Application of quantum machine learning using the quantum kernel algorithm on high energy physics analysis at the LHC, *Phys. Rev. Res.* **3**, 033221 (2021), [arXiv:2104.05059 \[quant-ph\]](#).
- [61] S. Zhang, Y.-C. Guo, and J.-C. Yang, Optimize the event selection strategy to study the anomalous quartic gauge couplings at muon colliders using the support vector machine and quantum support vector machine, *Eur. Phys. J. C* **84**, 833 (2024), [arXiv:2311.15280 \[hep-ph\]](#).
- [62] A. Fadol, Q. Sha, Y. Fang, Z. Li, S. Qian, Y. Xiao, Y. Zhang, and C. Zhou, Application of quantum machine learning in a Higgs physics study at the CEPC, *Int. J. Mod. Phys. A* **39**, 2450007 (2024), [arXiv:2209.12788 \[hep-ex\]](#).
- [63] S. Zhang, K.-X. Chen, and J.-C. Yang, Detect anomalous quartic gauge couplings at muon colliders with quantum kernel k-means (2024) [arXiv:2409.07010 \[hep-ph\]](#).
- [64] S. Weinberg, Baryon and Lepton Nonconserving Processes, *Phys. Rev. Lett.* **43**, 1566 (1979).
- [65] B. Grzadkowski, M. Iskrzynski, M. Misiak, and J. Rosiek, Dimension-Six Terms in the Standard Model Lagrangian, *JHEP* **10**, 085, [arXiv:1008.4884 \[hep-ph\]](#).
- [66] S. Willenbrock and C. Zhang, Effective Field Theory Beyond the Standard Model, *Ann. Rev. Nucl. Part. Sci.* **64**, 83 (2014), [arXiv:1401.0470 \[hep-ph\]](#).
- [67] E. Masso, An Effective Guide to Beyond the Standard Model Physics, *JHEP* **10**, 128, [arXiv:1406.6376 \[hep-ph\]](#).
- [68] P. T. Komiske, E. M. Metodiev, and J. Thaler, Metric Space of Collider Events, *Phys. Rev. Lett.* **123**, 041801 (2019), [arXiv:1902.02346 \[hep-ph\]](#).
- [69] M. Möttönen, J. J. Vartiainen, V. Bergholm, and M. M. Salomaa, Quantum Circuits for General Multiqubit Gates, *Phys. Rev. Lett.* **93**, 130502 (2004).
- [70] G. Brassard, P. Hoyer, M. Mosca, and A. Tapp, Quantum amplitude amplification and estimation (2000) [arXiv:quant-ph/0005055](#).
- [71] A. Kandala, A. Mezzacapo, K. Temme, M. Takita, M. Brink, J. M. Chow, and J. M. Gambetta, Hardware-efficient variational quantum eigensolver for small molecules and quantum magnets, *Nature* **549**, 242 (2017), [arXiv:1704.05018 \[quant-ph\]](#).
- [72] C. Bravo-Prieto, R. LaRose, M. Cerezo, Y. Subasi, L. Cincio, and P. J. Coles, Variational

- Quantum Linear Solver, *Quantum* **7**, 1188 (2023), [arXiv:1909.05820 \[quant-ph\]](#).
- [73] F. Pedregosa *et al.*, Scikit-learn: Machine Learning in Python, *J. Machine Learning Res.* **12**, 2825 (2011), [arXiv:1201.0490 \[cs.LG\]](#).
- [74] D. P. Kingma and J. Ba, Adam: A Method for Stochastic Optimization (2014) [arXiv:1412.6980 \[cs.LG\]](#).
- [75] C.-Y. Park, M. Kang, and J. Huh, Hardware-efficient ansatz without barren plateaus in any depth (2024) [arXiv:2403.04844 \[quant-ph\]](#).
- [76] T. Jones, A. Brown, I. Bush, and S. C. Benjamin, QuEST and High Performance Simulation of Quantum Computers, *Sci. Rep.* **9**, 10736 (2019).
- [77] Q. Zhu *et al.*, Quantum computational advantage via 60-qubit 24-cycle random circuit sampling, *Sci. Bull.* **67**, 240 (2022), [arXiv:2109.03494 \[quant-ph\]](#).
- [78] J. Alwall, R. Frederix, S. Frixione, V. Hirschi, F. Maltoni, O. Mattelaer, H. S. Shao, T. Stelzer, P. Torrielli, and M. Zaro, The automated computation of tree-level and next-to-leading order differential cross sections, and their matching to parton shower simulations, *JHEP* **07**, 079, [arXiv:1405.0301 \[hep-ph\]](#).
- [79] N. D. Christensen and C. Duhr, FeynRules - Feynman rules made easy, *Comput. Phys. Commun.* **180**, 1614 (2009), [arXiv:0806.4194 \[hep-ph\]](#).
- [80] C. Degrande, C. Duhr, B. Fuks, D. Grellscheid, O. Mattelaer, and T. Reiter, UFO - The Universal FeynRules Output, *Comput. Phys. Commun.* **183**, 1201 (2012), [arXiv:1108.2040 \[hep-ph\]](#).
- [81] T. Sjöstrand, S. Ask, J. R. Christiansen, R. Corke, N. Desai, P. Ilten, S. Mrenna, S. Prestel, C. O. Rasmussen, and P. Z. Skands, An introduction to PYTHIA 8.2, *Comput. Phys. Commun.* **191**, 159 (2015), [arXiv:1410.3012 \[hep-ph\]](#).
- [82] R. D. Ball, V. Bertone, S. Carrazza, L. Del Debbio, S. Forte, A. Guffanti, N. P. Hartland, and J. Rojo (NNPDF), Parton distributions with QED corrections, *Nucl. Phys. B* **877**, 290 (2013), [arXiv:1308.0598 \[hep-ph\]](#).
- [83] J. de Favereau, C. Delaere, P. Demin, A. Giammanco, V. Lemaître, A. Mertens, and M. Selvaggi (DELPHES 3), DELPHES 3, A modular framework for fast simulation of a generic collider experiment, *JHEP* **02**, 057, [arXiv:1307.6346 \[hep-ex\]](#).
- [84] Y.-C. Guo, F. Feng, A. Di, S.-Q. Lu, and J.-C. Yang, MLAnalysis: An open-source program for high energy physics analyses, *Comput. Phys. Commun.* **294**, 108957 (2024),

- [arXiv:2305.00964 \[hep-ph\]](#).
- [85] D. Donoho and J. Jin, Higher criticism for detecting sparse heterogeneous mixtures, *The Annals of Statistics* **32**, [10.1214/009053604000000265](#) (2004).
- [86] V. Havlicek, A. D. Córcoles, K. Temme, A. W. Harrow, A. Kandala, J. M. Chow, and J. M. Gambetta, Supervised learning with quantum-enhanced feature spaces, *Nature* **567**, [209](#) (2019), [arXiv:1804.11326 \[quant-ph\]](#).
- [87] S. Lloyd, M. Schuld, A. Ijaz, J. Izaac, and N. Killoran, Quantum embeddings for machine learning (2020) [arXiv:2001.03622 \[quant-ph\]](#).
- [88] P. A. Zyla *et al.* (Particle Data Group), Review of Particle Physics, *PTEP* **2020**, [083C01](#) (2020).
- [89] G. Cowan, K. Cranmer, E. Gross, and O. Vitells, Asymptotic formulae for likelihood-based tests of new physics, *Eur. Phys. J. C* **71**, [1554](#) (2011), [Erratum: *Eur.Phys.J.C* 73, 2501 (2013)], [arXiv:1007.1727 \[physics.data-an\]](#).
- [90] M. Born and L. Infeld, Foundations of the new field theory, *Proc. Roy. Soc. Lond. A* **144**, [425](#) (1934).
- [91] J. Ellis and S.-F. Ge, Constraining Gluonic Quartic Gauge Coupling Operators with  $gg \rightarrow \gamma\gamma$ , *Phys. Rev. Lett.* **121**, [041801](#) (2018), [arXiv:1802.02416 \[hep-ph\]](#).
- [92] J. Ellis, S.-F. Ge, and K. Ma, Hadron collider probes of the quartic couplings of gluons to the photon and Z boson, *JHEP* **04**, [123](#), [arXiv:2112.06729 \[hep-ph\]](#).
- [93] E. S. Fradkin and A. A. Tseytlin, Nonlinear Electrodynamics from Quantized Strings, *Phys. Lett. B* **163**, [123](#) (1985).
- [94] A. A. Tseytlin, Born-Infeld action, supersymmetry and string theory (1999) pp. 417–452, [arXiv:hep-th/9908105](#).
- [95] C. Cheung, K. Kampf, J. Novotny, C.-H. Shen, J. Trnka, and C. Wen, Vector Effective Field Theories from Soft Limits, *Phys. Rev. Lett.* **120**, [261602](#) (2018), [arXiv:1801.01496 \[hep-th\]](#).
- [96] D. R. Green, P. Meade, and M.-A. Pleier, Multiboson interactions at the LHC, *Rev. Mod. Phys.* **89**, [035008](#) (2017), [arXiv:1610.07572 \[hep-ex\]](#).
- [97] C. Zhang and S.-Y. Zhou, Convex Geometry Perspective on the (Standard Model) Effective Field Theory Space, *Phys. Rev. Lett.* **125**, [201601](#) (2020), [arXiv:2005.03047 \[hep-ph\]](#).
- [98] C. W. Murphy, Dimension-8 operators in the Standard Model Effective Field Theory, *JHEP* **10**, [174](#), [arXiv:2005.00059 \[hep-ph\]](#).

- [99] H.-L. Li, Z. Ren, J. Shu, M.-L. Xiao, J.-H. Yu, and Y.-H. Zheng, Complete set of dimension-eight operators in the standard model effective field theory, *Phys. Rev. D* **104**, 015026 (2021), [arXiv:2005.00008 \[hep-ph\]](#).
- [100] C. F. Anders *et al.*, Vector boson scattering: Recent experimental and theory developments, *Rev. Phys.* **3**, 44 (2018), [arXiv:1801.04203 \[hep-ph\]](#).
- [101] B. Henning, X. Lu, T. Melia, and H. Murayama, 2, 84, 30, 993, 560, 15456, 11962, 261485, ...: Higher dimension operators in the SM EFT, *JHEP* **08**, 016, [Erratum: *JHEP* 09, 019 (2019)], [arXiv:1512.03433 \[hep-ph\]](#).
- [102] C. Zhang and S.-Y. Zhou, Positivity bounds on vector boson scattering at the LHC, *Phys. Rev. D* **100**, 095003 (2019), [arXiv:1808.00010 \[hep-ph\]](#).
- [103] Q. Bi, C. Zhang, and S.-Y. Zhou, Positivity constraints on aQGC: carving out the physical parameter space, *JHEP* **06**, 137, [arXiv:1902.08977 \[hep-ph\]](#).
- [104] M. Aaboud *et al.* (ATLAS), Studies of  $Z\gamma$  production in association with a high-mass dijet system in  $pp$  collisions at  $\sqrt{s} = 8$  TeV with the ATLAS detector, *JHEP* **07**, 107, [arXiv:1705.01966 \[hep-ex\]](#).
- [105] V. Khachatryan *et al.* (CMS), Measurement of the cross section for electroweak production of  $Z\gamma$  in association with two jets and constraints on anomalous quartic gauge couplings in proton–proton collisions at  $\sqrt{s} = 8$  TeV, *Phys. Lett. B* **770**, 380 (2017), [arXiv:1702.03025 \[hep-ex\]](#).
- [106] A. M. Sirunyan *et al.* (CMS), Measurement of the cross section for electroweak production of a Z boson, a photon and two jets in proton-proton collisions at  $\sqrt{s} = 13$  TeV and constraints on anomalous quartic couplings, *JHEP* **06**, 076, [arXiv:2002.09902 \[hep-ex\]](#).
- [107] V. Khachatryan *et al.* (CMS), Measurement of electroweak-induced production of  $W\gamma$  with two jets in  $pp$  collisions at  $\sqrt{s} = 8$  TeV and constraints on anomalous quartic gauge couplings, *JHEP* **06**, 106, [arXiv:1612.09256 \[hep-ex\]](#).
- [108] A. M. Sirunyan *et al.* (CMS), Measurement of vector boson scattering and constraints on anomalous quartic couplings from events with four leptons and two jets in proton–proton collisions at  $\sqrt{s} = 13$  TeV, *Phys. Lett. B* **774**, 682 (2017), [arXiv:1708.02812 \[hep-ex\]](#).
- [109] A. M. Sirunyan *et al.* (CMS), Measurement of differential cross sections for Z boson pair production in association with jets at  $\sqrt{s} = 8$  and 13 TeV, *Phys. Lett. B* **789**, 19 (2019), [arXiv:1806.11073 \[hep-ex\]](#).

- [110] M. Aaboud *et al.* (ATLAS), Observation of electroweak  $W^\pm Z$  boson pair production in association with two jets in  $pp$  collisions at  $\sqrt{s} = 13$  TeV with the ATLAS detector, *Phys. Lett. B* **793**, 469 (2019), [arXiv:1812.09740 \[hep-ex\]](#).
- [111] A. M. Sirunyan *et al.* (CMS), Measurement of electroweak WZ boson production and search for new physics in WZ + two jets events in pp collisions at  $\sqrt{s} = 13$  TeV, *Phys. Lett. B* **795**, 281 (2019), [arXiv:1901.04060 \[hep-ex\]](#).
- [112] V. Khachatryan *et al.* (CMS), Evidence for exclusive  $\gamma\gamma \rightarrow W^+W^-$  production and constraints on anomalous quartic gauge couplings in  $pp$  collisions at  $\sqrt{s} = 7$  and 8 TeV, *JHEP* **08**, 119, [arXiv:1604.04464 \[hep-ex\]](#).
- [113] A. M. Sirunyan *et al.* (CMS), Observation of electroweak production of same-sign W boson pairs in the two jet and two same-sign lepton final state in proton-proton collisions at  $\sqrt{s} = 13$  TeV, *Phys. Rev. Lett.* **120**, 081801 (2018), [arXiv:1709.05822 \[hep-ex\]](#).
- [114] J. Ellis, H.-J. He, and R.-Q. Xiao, Probing Neutral Triple Gauge Couplings with  $Z^*\gamma(\nu\bar{\nu}\gamma)$  Production at Hadron Colliders (2023) [arXiv:2308.16887 \[hep-ph\]](#).
- [115] S. Spor, Probe of the anomalous neutral triple gauge couplings in photon-induced collision at future muon colliders, *Nucl. Phys. B* **991**, 116198 (2023), [arXiv:2207.11585 \[hep-ph\]](#).
- [116] S. Spor, E. Gurkanli, and M. Köksal, Search for the anomalous  $ZZ\gamma$  and  $Z\gamma\gamma$  couplings via  $\nu\nu\gamma$  production at the CLIC, *Nucl. Phys. B* **979**, 115785 (2022), [arXiv:2203.02352 \[hep-ph\]](#).
- [117] A. Yilmaz, Search for the limits on anomalous neutral triple gauge couplings via ZZ production in the  $ll\nu\nu$  channel at FCC-hh, *Nucl. Phys. B* **969**, 115471 (2021), [arXiv:2102.01989 \[hep-ph\]](#).
- [118] J. Ellis, H.-J. He, and R.-Q. Xiao, Probing new physics in dimension-8 neutral gauge couplings at  $e^+e^-$  colliders, *Sci. China Phys. Mech. Astron.* **64**, 221062 (2021), [arXiv:2008.04298 \[hep-ph\]](#).
- [119] A. Senol, H. Denizli, A. Yilmaz, I. Turk Cakir, and O. Cakir, Study on Anomalous Neutral Triple Gauge Boson Couplings from Dimension-eight Operators at the HL-LHC (2019) [arXiv:1906.04589 \[hep-ph\]](#).
- [120] A. Yilmaz, A. Senol, H. Denizli, I. Turk Cakir, and O. Cakir, Sensitivity on Anomalous Neutral Triple Gauge Couplings via ZZ Production at FCC-hh, *Eur. Phys. J. C* **80**, 173 (2020), [arXiv:1906.03911 \[hep-ph\]](#).
- [121] J. Ellis, S.-F. Ge, H.-J. He, and R.-Q. Xiao, Probing the scale of new physics in the  $ZZ\gamma$

- coupling at  $e^+e^-$  colliders, [Chin. Phys. C \*\*44\*\*, 063106 \(2020\)](#), [arXiv:1902.06631 \[hep-ph\]](#).
- [122] S. Jahedi and J. Lahiri, Probing anomalous  $ZZ\gamma$  and  $Z\gamma\gamma$  couplings at the  $e^+e^-$  colliders using optimal observable technique, [JHEP \*\*04\*\*, 085](#), [arXiv:2212.05121 \[hep-ph\]](#).
- [123] S. Jahedi, Optimal estimation of Dimension-8 Neutral Triple Gauge Couplings at  $e^+e^-$  Colliders (2023) [arXiv:2305.11266 \[hep-ph\]](#).
- [124] J.-C. Yang, Y.-C. Guo, and Y.-F. Dong, Study of the gluonic quartic gauge couplings at muon colliders (2023) p. 115201, [arXiv:2307.04207 \[hep-ph\]](#).
- [125] K. M. Black *et al.*, Muon Collider Forum report, [JINST \*\*19\*\* \(02\), T02015](#), [arXiv:2209.01318 \[hep-ex\]](#).
- [126] C. Accettura *et al.*, Towards a muon collider, [Eur. Phys. J. C \*\*83\*\*, 864 \(2023\)](#), [Erratum: [Eur.Phys.J.C 84, 36 \(2024\)](#)], [arXiv:2303.08533 \[physics.acc-ph\]](#).
- [127] M. Czakon and A. Mitov, Top++: A Program for the Calculation of the Top-Pair Cross-Section at Hadron Colliders, [Comput. Phys. Commun. \*\*185\*\*, 2930 \(2014\)](#), [arXiv:1112.5675 \[hep-ph\]](#).
- [128] A. M. Sirunyan *et al.* (CMS), Measurement of the cross section for  $t\bar{t}$  production with additional jets and b jets in pp collisions at  $\sqrt{s} = 13$  TeV, [JHEP \*\*07\*\*, 125](#), [arXiv:2003.06467 \[hep-ex\]](#).
- [129] G. Aad *et al.* (ATLAS), Measurement of  $t\bar{t}$  production in association with additional  $b$ -jets in the  $e\mu$  final state in proton-proton collisions at  $\sqrt{s}=13$  TeV with the ATLAS detector (2024) [arXiv:2407.13473 \[hep-ex\]](#).
- [130] S. Sim, P. D. Johnson, and A. Aspuru-Guzik, Expressibility and Entangling Capability of Parameterized Quantum Circuits for Hybrid Quantum-Classical Algorithms, [Adv. Quantum Technol. \*\*2\*\*, 1900070 \(2019\)](#), [arXiv:1905.10876 \[quant-ph\]](#).
- [131] G. Aad *et al.* (ATLAS), ATLAS  $b$ -jet identification performance and efficiency measurement with  $t\bar{t}$  events in pp collisions at  $\sqrt{s} = 13$  TeV, [Eur. Phys. J. C \*\*79\*\*, 970 \(2019\)](#), [arXiv:1907.05120 \[hep-ex\]](#).
- [132] Y.-C. Guo, Y.-Y. Wang, and J.-C. Yang, Constraints on anomalous quartic gauge couplings by  $\gamma\gamma \rightarrow W^+W^-$  scattering, [Nucl. Phys. B \*\*961\*\*, 115222 \(2020\)](#), [arXiv:1912.10686 \[hep-ph\]](#).
- [133] Y.-F. Dong, Y.-C. Mao, and J.-C. Yang, Searching for anomalous quartic gauge couplings at muon colliders using principal component analysis, [Eur. Phys. J. C \*\*83\*\*, 555 \(2023\)](#), [arXiv:2304.01505 \[hep-ph\]](#).

- [134] J.-C. Yang, Y.-C. Guo, C.-X. Yue, and Q. Fu, Constraints on anomalous quartic gauge couplings via  $Z\gamma jj$  production at the LHC, *Phys. Rev. D* **104**, 035015 (2021), [arXiv:2107.01123 \[hep-ph\]](#).
- [135] Y.-C. Guo, Y.-Y. Wang, J.-C. Yang, and C.-X. Yue, Constraints on anomalous quartic gauge couplings via  $W\gamma jj$  production at the LHC, *Chin. Phys. C* **44**, 123105 (2020), [arXiv:2002.03326 \[hep-ph\]](#).
- [136] C.-X. Yue, X.-J. Cheng, and J.-C. Yang, Charged-current non-standard neutrino interactions at the LHC and HL-LHC\*, *Chin. Phys. C* **47**, 043111 (2023), [arXiv:2110.01204 \[hep-ph\]](#).
- [137] Q. Fu, J.-C. Yang, C.-X. Yue, and Y.-C. Guo, The study of neutral triple gauge couplings in the process  $e+e\rightarrow Z\gamma$  including unitarity bounds, *Nucl. Phys. B* **972**, 115543 (2021), [arXiv:2102.03623 \[hep-ph\]](#).
- [138] J.-C. Yang, Y.-C. Guo, B. Liu, and T. Li, Shining light on magnetic monopoles through high-energy muon colliders, *Nucl. Phys. B* **987**, 116097 (2023), [arXiv:2208.02188 \[hep-ph\]](#).
- [139] J. Layssac, F. M. Renard, and G. J. Gounaris, Unitarity constraints for transverse gauge bosons at LEP and supercolliders, *Phys. Lett. B* **332**, 146 (1994), [arXiv:hep-ph/9311370](#).
- [140] T. Corbett, O. J. P. Éboli, and M. C. Gonzalez-Garcia, Unitarity Constraints on Dimension-six Operators II: Including Fermionic Operators, *Phys. Rev. D* **96**, 035006 (2017), [arXiv:1705.09294 \[hep-ph\]](#).
- [141] G. Perez, M. Sekulla, and D. Zeppenfeld, Anomalous quartic gauge couplings and unitarization for the vector boson scattering process  $pp \rightarrow W^+W^+jjX \rightarrow \ell^+\nu_\ell\ell^+\nu_\ell jjX$ , *Eur. Phys. J. C* **78**, 759 (2018), [arXiv:1807.02707 \[hep-ph\]](#).
- [142] E. d. S. Almeida, O. J. P. Éboli, and M. C. Gonzalez-Garcia, Unitarity constraints on anomalous quartic couplings, *Phys. Rev. D* **101**, 113003 (2020), [arXiv:2004.05174 \[hep-ph\]](#).
- [143] W. Kilian, S. Sun, Q.-S. Yan, X. Zhao, and Z. Zhao, Multi-Higgs boson production and unitarity in vector-boson fusion at future hadron colliders, *Phys. Rev. D* **101**, 076012 (2020), [arXiv:1808.05534 \[hep-ph\]](#).
- [144] W. Kilian, S. Sun, Q.-S. Yan, X. Zhao, and Z. Zhao, Highly Boosted Higgs Bosons and Unitarity in Vector-Boson Fusion at Future Hadron Colliders, *JHEP* **05**, 198, [arXiv:2101.12537 \[hep-ph\]](#).
- [145] J. Chang, K. Cheung, C.-T. Lu, and T.-C. Yuan, WW scattering in the era of post-Higgs-boson discovery, *Phys. Rev. D* **87**, 093005 (2013), [arXiv:1303.6335 \[hep-ph\]](#).

- [146] G. Aad *et al.* (ATLAS), Evidence for Electroweak Production of  $W^\pm W^\pm jj$  in  $pp$  Collisions at  $\sqrt{s} = 8$  TeV with the ATLAS Detector, *Phys. Rev. Lett.* **113**, 141803 (2014), [arXiv:1405.6241 \[hep-ex\]](#).
- [147] A. M. Sirunyan *et al.* (CMS), Measurements of production cross sections of WZ and same-sign WW boson pairs in association with two jets in proton-proton collisions at  $\sqrt{s} = 13$  TeV, *Phys. Lett. B* **809**, 135710 (2020), [arXiv:2005.01173 \[hep-ex\]](#).
- [148] A. M. Sirunyan *et al.* (CMS), Search for anomalous electroweak production of vector boson pairs in association with two jets in proton-proton collisions at 13 TeV, *Phys. Lett. B* **798**, 134985 (2019), [arXiv:1905.07445 \[hep-ex\]](#).
- [149] A. M. Sirunyan *et al.* (CMS), Observation of electroweak production of  $W\gamma$  with two jets in proton-proton collisions at  $\sqrt{s} = 13$  TeV, *Phys. Lett. B* **811**, 135988 (2020), [arXiv:2008.10521 \[hep-ex\]](#).
- [150] A. M. Sirunyan *et al.* (CMS), Evidence for electroweak production of four charged leptons and two jets in proton-proton collisions at  $\sqrt{s} = 13$  TeV, *Phys. Lett. B* **812**, 135992 (2021), [arXiv:2008.07013 \[hep-ex\]](#).
- [151] J.-C. Yang, Z.-B. Qing, X.-Y. Han, Y.-C. Guo, and T. Li, Tri-photon at muon collider: a new process to probe the anomalous quartic gauge couplings, *JHEP* **22**, 053, [arXiv:2204.08195 \[hep-ph\]](#).
- [152] O. J. P. Eboli, M. C. Gonzalez-Garcia, and J. K. Mizukoshi,  $p p \rightarrow j j e^+ e^- \mu^+ \mu^- \nu \nu$  and  $j j e^+ e^- \mu^+ \nu \nu$  at  $O(\alpha(\text{em})^6)$  and  $O(\alpha(\text{em})^4 \alpha(s)^2)$  for the study of the quartic electroweak gauge boson vertex at CERN LHC, *Phys. Rev. D* **74**, 073005 (2006), [arXiv:hep-ph/0606118](#).
- [153] O. J. P. Éboli and M. C. Gonzalez-Garcia, Classifying the bosonic quartic couplings, *Phys. Rev. D* **93**, 093013 (2016), [arXiv:1604.03555 \[hep-ph\]](#).
- [154] A. Abada *et al.* (FCC), HE-LHC: The High-Energy Large Hadron Collider: Future Circular Collider Conceptual Design Report Volume 4, *Eur. Phys. J. ST* **228**, 1109 (2019).
- [155] M. Benedikt *et al.*, Future Circular Hadron Collider FCC-hh: Overview and Status (2022) [arXiv:2203.07804 \[physics.acc-ph\]](#).